RESEARCH ARTICLE

Key Points:
- The onshore heat transport is coupled to the offshore zonal wind stress
- The seasonal cycle of ice-shelf melting depends on its thickness distribution
- Asymmetric response to change in ocean heat transport enhances ice-shelf melting

Oceanographic Controls on the Variability of Ice-Shelf Basal Melting and Circulation of Glacial Meltwater in the Amundsen Sea Embayment, Antarctica

Satoshi Kimura[1,2,3] [iD], Adrian Jenkins[1] [iD], Heather Regan[1,4] [iD], Paul R. Holland[1], Karen M. Assmann[5] [iD], Daniel B. Whitt[6] [iD], Melchoir Van Wessem[7], Willem Jan van de Berg[7] [iD], Carleen H. Reijmer[7] [iD], and Pierre Dutrieux[8] [iD]

[1]British Antarctic Survey, Natural Environment Research Council, Cambridge, UK, [2]Nansen Environmental and Remote Sensing Center and Bjerknes Centre for Climate Research, Bergen, Norway, [3]Japan Agency for Marine-Earth Science and Technology, Natsushima-cho, Yokosuka, Japan, [4]School of Earth and Ocean Sciences, Cardiff University, Cardiff, UK, [5]Department of Marine Sciences, University of Gothenburg, Gothenburg, Sweden, [6]National Center for Atmospheric Research, Boulder, CO, USA, [7]Institute for Marine and Atmospheric Research, Department of Physics and Astronomy, Faculty of Science, Utrecht University, Utrecht, The Netherlands, [8]Lamont-Doherty Earth Observatory, Columbia University, Palisades, NY, USA

Abstract Ice shelves in the Amundsen Sea Embayment have thinned, accelerating the seaward flow of ice sheets upstream over recent decades. This imbalance is caused by an increase in the ocean-driven melting of the ice shelves. Observations and models show that the ocean heat content reaching the ice shelves is sensitive to the depth of thermocline, which separates the cool, fresh surface waters from warm, salty waters. Yet the processes controlling the variability of thermocline depth remain poorly constrained. Here we quantify the oceanic conditions and ocean-driven melting of Cosgrove, Pine Island Glacier (PIG), Thwaites, Crosson, and Dotson ice shelves in the Amundsen Sea Embayment from 1991 to 2014 using a general circulation model. Ice-shelf melting is coupled to variability in the wind field and the sea-ice motions over the continental shelf break and associated onshore advection of warm waters in deep troughs. The layer of warm, salty waters at the calving front of PIG and Thwaites is thicker in austral spring (June–October) than in austral summer (December–March), whereas the seasonal cycle at the calving front of Dotson is reversed. Furthermore, the ocean-driven melting in PIG is enhanced by an asymmetric response to changes in ocean heat transport anomalies at the continental shelf break: melting responds more rapidly to increases in ocean heat transport than to decreases. This asymmetry is caused by the inland deepening of bathymetry and the glacial meltwater circulation around the ice shelf.

1. Introduction

Ice shelves (the floating extensions of grounded ice sheets) are at the forefront of ice sheet-ocean interactions in Antarctica, mediating the release of grounded ice to the ocean. Unsteady ocean-driven melting of the ice shelves reduces the restraint on the flow of grounded ice sheets upstream (Gudmundsson, 2013; Schoof, 2007) and structurally weakens the ice shelves by carving channels into their undersides (Alley et al., 2016; Dutrieux et al., 2013; Gladish et al., 2012; Millgate et al., 2013; Rignot & Steffen, 2008), leading to an increase in discharge of the grounded ice into the ocean. This implies that the state of individual ice shelves has an ability to alter the evolution of the Antarctic ice sheet as a whole and therefore underpins our prediction of sea level rise (Rye et al., 2014), the ocean freshwater budget (Jacobs et al., 2002), and the rate of global deepwater ventilation (Purkey & Johnson, 2012).

The Amundsen Sea Embayment hosts many of the most rapidly thinning ice shelves in Antarctica (Paolo et al., 2015; Pritchard et al., 2012). In particular, Pine Island Glacier (PIG) and its neighboring Thwaites Glacier have been highlighted as major drainage pathways for the West Antarctic Ice Sheet. The rapid thinning of the ice shelves is almost certainly due to an unsteady ocean-driven melting (Payne et al., 2004; Shepherd et al., 2004). The heat that fuels the unsteady melting resides in slightly modified Circumpolar Deep Water (CDW) on the continental shelf in the Amundsen Sea (Dutrieux et al., 2014; Jacobs et al., 1996, 2011;

Walker et al., 2007). The CDW is a few degrees above the in situ freezing point, and increasing the rate of intrusion of this water mass into the sub-ice-shelf cavity gives rise to rapid ocean-driven melting of PIG (Jenkins et al., 2010).

In response to this increased melting, PIG and Thwaites will gradually lose mass, potentially leading to an irreversible collapse of the West Antarctic Ice Sheet (Favier et al., 2014; Joughin et al., 2014). A key uncertainty that hinders the prediction of such a collapse lies in ice-ocean interactions within the current century. Despite this importance, our knowledge of interannual oceanic variability and its link to the ice-shelf melting in the Amundsen Sea Embayment is limited to intermittent summer-months observations starting from 1994 (Dutrieux et al., 2014; Jacobs et al., 1996, 2011) and continuous mooring records of only 2–5 years (Assmann et al., 2013; Wåhlin et al., 2013; Webber et al., 2017).

We assess the interannual variability of ice-shelf melting and its connection to the regional ocean circulation in the Amundsen Sea with an eddy-permitting ocean model forced with two different sets of atmospheric boundary conditions (ERA-Interim and RACMO2.3) from 1991 to 2014. Our goal is to expand our understanding of the processes that regulate interannual variability of ice-shelf melting in the Amundsen Sea Embayment over recent decades and to provide a broader context for the interpretation of modeling and observational estimates of the ice-shelf melting. The model configuration is described in section 2. Section 3 presents the climatology of the model results. The model's seasonal cycle and interannual variability of the onshore heat transport and ice-shelf melting are described in sections 4 and 5. Section 6 discusses the effects of the atmospheric forcing on the onshore heat transport. Finally, our discussion and conclusions are summarized in sections 7 and 8.

2. Methodology

We employ revision c62r of the Massachusetts Institute of Technology general circulation model (MITgcm; http://mitgcm.org) adapted to include sub-ice-shelf cavities (Losch, 2008) and coupled with a sea-ice model based on a viscous-plastic rheology (Losch et al., 2010). The ocean component of the model solves the rotating hydrostatic Boussinesq equations and advection-diffusion equations for temperature and salinity on a generalized curvilinear grid using an Arakawa C-grid finite-volume method and z levels in the vertical (Marshall et al., 1997). All the prognostic variables are solved with the horizontal resolution of 0.1° in longitude, producing approximately square cells ranging from ∼2.8 km on each side at the southern end of the domain to ∼5.2 km at the northern end of the domain. The vertical component is discretized into 50 vertical levels ranging from 10 m resolution near the top to 200 m near the bottom. The steplike representations of seabed and ice-shelf topography are alleviated by the use of partial cells outlined in Adcroft et al. (1997). The model domain covers the Amundsen Sea Embayment between 75.5°S and 62°S and 140°W and 80°W, which includes eight ice shelves (Getz, Dotson, Crosson, Thwaites, PIG, Cosgrove, Abbot, and Venable ice shelves; Figure 1). There is no explicit horizontal diffusion for temperature and salinity fields, and vertical diffusion is parameterized using the K-profile parameterization (KPP) scheme (Large et al., 1994). The equation of state is represented using an algorithm described in McDougall et al. (2003). The volume fractions of freshwater sources in the model (precipitation, evaporation, surface runoff, glacial meltwater, and sea-ice salt flux) are tracked as passive tracers (Regan et al., 2017).

Initial conditions for ocean temperature and salinity are constructed by interpolating the World Ocean Atlas onto the model grid, and seabed and ice-shelf topography are derived from the global 1 min Refined Topography data set (RTOPO; Timmermann et al., 2010). Steady climatological conditions for velocity, temperature, and salinity from the Southern Ocean model described in Holland et al. (2014) are applied at the northern, western, and eastern boundaries. The model starts by applying the atmospheric forcing in January 1991 and ends in December 2014. The propagations of temperature signals from the continental shelf break to the calving front at the beginning of the simulation take about 1 year. The regional spin-up is effectively done after 1 year, and we regard the model as being spun up after 1994. The effects of the atmospheric seasonal cycle are present during the spin-up period (1991–1994), so we do not exclude the spin-up period for analyzing the modeled seasonal cycle and interannual variabilities.

We use two sets of atmospheric forcing conditions, ERA-Interim and RACMO2.3. The atmospheric forcing variables consist of zonal and meridional 10 m winds, 2 m air temperature and specific humidity, downward
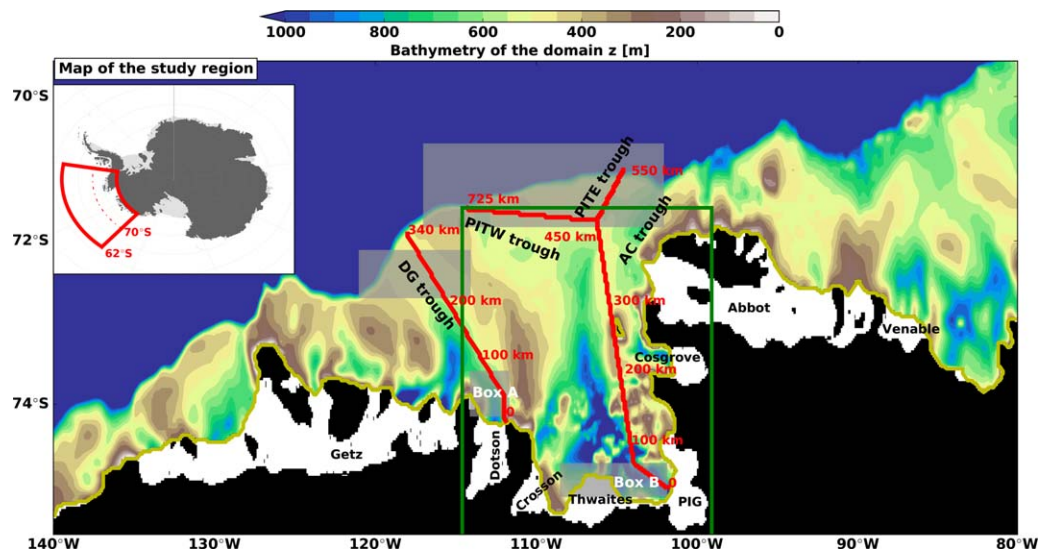
Figure 1. A map of the bathymetry in a portion of the model domain. The names of bathymetric troughs are Abbot-Cosgrove (AC), Pine Island-Thwaites East (PITE), Pine Island-Thwaites West (PITW), and Dotson-Getz trough (DG) as in Smith et al. (2014). The shaded areas along the continental shelf break indicate the regions over the DG and PITW/PITE troughs used to derive mean wind field in Figures 6a and 6b. The shaded areas along the coastline show the Dotson calving front, box A, and PIG/Thwaites calving fronts, box B. The region enclosed by the green lines indicates Pine Island Bay. The three red lines indicate the transect lines used for Hovmöller plots in Figures 7b–7d.

shortwave and longwave radiation, and precipitation. These forcing fields from ERA-Interim or RACMO2.3 are applied on the surface of the ocean model using 6-hourly fields.

ERA-Interim is a global atmospheric reanalysis from 1979 to the present developed at the European Centre for Medium-Range Weather Forecasts (ECMWF) at a resolution of 0.75° in both longitude and latitude (Dee et al., 2011). ERA-Interim is the most reliable reanalysis out of five different reanalysis data sets over three decades spanning 1979–2008 when verified over Antarctica against independent surface and midtropospheric pressure and temperature observations (Bracegirdle & Marshall, 2012). RACMO2.3 is a regional atmospheric climate model adapted for use over the Antarctic continent and is forced by ERA-Interim reanalyses at its lateral boundaries. RACMO2.3 is hydrostatic and is run at a relatively high horizontal resolution of 27 km and a vertical resolution of 40 levels (Van Wessem et al., 2014). The interior of the domain is not constrained toward observations and therefore allowed to evolve freely. The higher resolution in RACMO2.3 (27 km versus ≈80 km) has a better representation of the coastline, and we expect RACMO2.3 to capture the atmospheric variability near the calving front of ice shelves.

3. Overview

The Amundsen Sea Embayment is characterized by relatively warm, salty water offshore of the continental slope with cooler and fresher water residing over the continental shelf (Dutrieux et al., 2014; Jacobs et al., 1996). The continental shelf acts as a topographic barrier for delivering warm water to floating ice shelves. Any significant topographic depressions in the continental shelf break or climatic forcing that changes the height of the warmest water will affect the transport of heat onto the shelf. The modeled ocean circulation is broadly consistent with the observations. The observations indicate the onshore deflection of an eastward undercurrent along the continental shelf at the PITW trough, which connects the continental shelf break and ice shelves (Assmann et al., 2013; Walker et al., 2013). These deep trough-guided onshore inflows of the warm waters, a few degrees above freezing point, are captured in the model within all the Amundsen Sea troughs (Figure 2a).

We compare the climatological melt rates to the previous modeling studies and observations. The modeled melt rates are often expressed by the ice thickness change per year (m yr^{-1}), whereas the unit of gigatons of ice loss per year (Gt yr^{-1}) is commonly used in the observations. Converting the unit from m yr^{-1} to
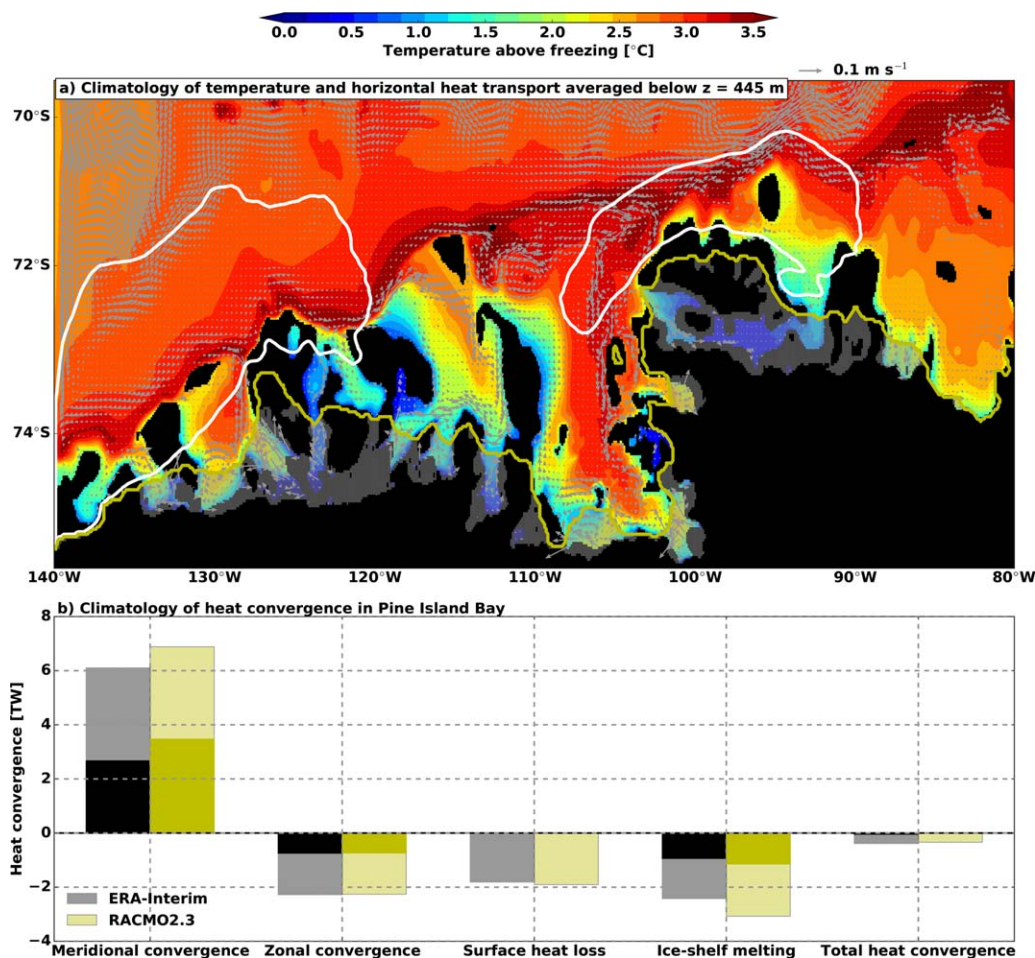
Figure 2. (a) Climatology of temperature above freezing averaged below 447.5 m (color scale) and horizontal velocity vectors at 447.5 m (arrows, plotted every four grid points) from ERA-Interim forced simulation. The white contours indicate the regions with the climatological sea-ice concentration higher than 0.75. (b) The climatological heat convergence terms from ERA-Interim and RACMO2.3 forced simulations. The darker portions of the bar chart indicate the heat convergence below 447.5 m.

Gt yr^{-1} requires a precise knowledge of the ice-shelf geometry used in the model, which we do not have for the previous model studies. Our melt rates in m yr^{-1} are compared with the previous modeling studies, and our melt rates are converted to Gt yr^{-1} for comparisons with the observations (Table 1). We also list the ice-shelf area used in our model in Table 1. Climatological melt rates differ considerably among the eight ice shelves. The RACMO2.3 simulation has slightly higher climatological melt rates than the ERA-Interim simulation, with less variability in all the ice shelves. Three of the fastest melting ice shelves in our model are Cosgrove, PIG, and Thwaites, where deep warm waters penetrate inside the ice-shelf cavities (Figure 2a). While many model results show that PIG and Thwaites are the two fastest melting ice shelves, the differences among the models are large. This is somewhat expected due to the different modeled years, resolutions, model formulations, atmospheric forcing, and domain geometry. Our modeled melt rates compare well with the results of St-Laurent et al. (2015) except in Crosson, where it is 5 times higher than our results. The model of St-Laurent et al. (2015) derives the domain geometry from IBCSO (Arndt et al., 2013) and BEDMAP-2 (Fretwell et al., 2013), and their bathymetry along the western side of Crosson is deeper than our RTOPO derived bathymetry. The Crosson ice-shelf cavity in the model of St-Laurent et al. (2015) has a better access to the warm deep waters than our model, which gives rise to the higher melting in Crosson. Our modeled PIG melt rates of 14–17 m yr^{-1} are in the similar range to St-Laurent et al. (2015; 15 m yr^{-1}) but higher than Nakayama et al. (2014; 6.6 m yr^{-1}) and lower than Schodlok et al. (2012; 28.3 m yr^{-1}).

Table 1
Comparison of Our Climatological Melt Rates to the Previous Modeled Melt Rates and Observed Melt Rates

	Getz	Dotson	Crosson	Thwaites	PIG	Cosgrove	Abbot	Venable
Ice-shelf area in our model (km^2)	36,785.3	5,269.5	2,534.5	4,960.9	6,087.5	3,145	35,626.4	3,625.2
ERA-Interim[a] (m yr^{-1})	7.6 ± 2.1	2.7 ± 1.2	0.9 ± 0.7	12.6 ± 3.8	14.1 ± 4.3	13.1 ± 5.7	1.4 ± 1.2	10.7 ± 3.6
RACMO2.3[a] (m yr^{-1})	9.5 ± 1.4	3.4 ± 1.1	1.0 ± 0.7	15.0 ± 2.7	17.4 ± 2.1	17.5 ± 2.9	2.5 ± 1.1	13.5 ± 3.2
St-Laurent et al. (2015)[b] (m yr^{-1})	7.6 ± 1	4.1 ± 0.5	5.0 ± 0.2	21.0 ± 2.0	15.2 ± 1	7.0 ± 0.5	1.8 ± 0.1	
Nakayama et al. (2014)[c] (m yr^{-1})	3.8				6.6		1.8	
Schodlok et al. (2012)[d] (m yr^{-1})	23.0	18.2	8.0	14.8	28.3	15.8	5.6	
ERA-Interim[a] (Gt yr^{-1})	257 ± 71	13 ± 5	2 ± 1	57 ± 17	78 ± 24	37 ± 16	45 ± 39	35 ± 12
RACMO2.3[a] (Gt yr^{-1})	321 ± 47	16 ± 5	2 ± 1	68 ± 12	97 ± 11	97 ± 11	81 ± 36	45 ± 10
Depoorter et al. (2013)[e] (Gt yr^{-1})	136 ± 23	78 ± 7		69 ± 18	95 ± 14	11 ± 3	86 ± 22	15 ± 3
Rignot et al. (2013)[f] (Gt yr^{-1})	145 ± 14	45 ± 4	39 ± 4	98 ± 7	101 ± 8	9 ± 2	52 ± 19	19 ± 2
Jacobs et al. (2013)[g] (Gt yr^{-1})	37–137							
Dutrieux et al. (2014)[h] (Gt yr^{-1})					34–102			

[a]Years 1991–2014 in our simulation. The ± represents one standard deviation away from the climatology.
[b]Modeled melt rates in years 2007–2013.
[c]Modeled melt rates in years 1984–1998.
[d]Modeled melt rates in years 1981–2010.
[e]Satellite based estimate. Melting of Crosson is included in Dotson melting.
[f]Satellite based estimate.
[g]Oceanographic estimates in 2000 (37 Gt yr^{-1}) and 2007 (137 Gt yr^{-1}).
[h]Oceanographic estimates in 1994 (47 Gt yr^{-1}), 2007 (102 Gt yr^{-1}), 2009 (73 Gt yr^{-1}), 2010 (69 Gt yr^{-1}), and 2012 (34 Gt yr^{-1}).

Our PIG melt rates are within the range of the observed melt rates, but the ice-shelf melt rates near the lateral boundaries of the model (Getz and Venerable) tend to be higher than the observations. While representations of ice-shelf cavity geometry are important in determining the circulation beneath the ice shelves and the melt rates (e.g., De Rydt et al., 2014; Holland et al., 2008), the ice-shelf cavity geometries are not well constrained due to a lack of observations. An important exception is PIG, where the geometry of the ice-shelf cavity is interpolated from the data acquired by sending an autonomous underwater vehicle beneath the ice shelf (Jenkins et al., 2010). It may be possible to modify the parameters controlling ice/ocean exchanges to better match observed melt rate (e.g., Jourdain et al., 2017), but such an exercise is inherently perilous and would not guarantee a better representation of the melt sensitivity to ocean properties. To investigate what drives changes in ocean heat content available to melt the ice, we assume hereafter that a perfect representation of melt rates is not necessary.

The climatological heat convergence (normalized by the in situ freezing temperature) from the ERA-Interim and RACMO2.3 forced simulations is very similar (Figure 2b). The heat convergence is defined as a time rate of change in thermal driving, $\frac{\partial}{\partial t}\left[\rho C_p(T - T_f)\right]$, where ρ and C_p are density and specific heat capacity of seawater. The variables T and T_f are temperature and its freezing point, respectively. Melting of ice shelves occurs by consuming the heat above in situ melting point, so the reference temperature of the onshore heat transport is set to the in situ freezing point, a linear function of salinity. The net heat convergence in the model consists of five terms: (1) advection, (2) diffusion, (3) KPP (parameterized vertical mixing), (4) surface heat flux, and (5) ice-shelf melting. The advection and diffusion terms include the horizontal and vertical components. The heat convergence is calculated inside the green box in Figure 1, which we refer to as "Pine Island Bay." When these five terms are calculated inside the green box (integrated over horizontal and vertical directions), the following terms survive: (1) meridional convergence, (2) zonal convergence, (3) surface heat loss, and (4) ice-shelf melting. The green box is chosen such that there are no inflows from the southern boundary. As a result, the meridional heat convergence is equal to the onshore meridional heat transport from the north. The meridional onshore inflow is the only source of heat into Pine Island Bay on a climatological mean. In total, the meridional onshore heat transport supplies heat to Pine Island Bay at a rate of 6.2 Terawatt (TW) and 6.8 TW in the ERA-Interim and RACMO2.3 forced simulations, respectively, and about half of the heat enters below 447.5 m (Figure 2b). Heat is lost at a rate of 2.4 TW in the zonal direction and is transferred to the atmosphere above Pine Island Bay at a rate of 1.9 TW in both simulations. Ice-shelf melting of Dotson, Crosson, Thwaites, PIG, Cosgrove, and the western side of Abbot ice shelves consumes the remaining 2.4 TW (ERA-Interim) and 3 TW (RACMO2.3).

4. Seasonal Cycle

Our knowledge of the seasonal cycle of ice-shelf melting and its connection to the external forcing factors is hampered by (1) the limited ship access to the Amundsen Sea Embayment, which can only take place in the summer months and (2) the lack of moored observations in the upper water column to avoid collisions with icebergs. Here we assess the modeled mean seasonal cycle during 1991–2014.

The onshore heat transport is defined as the transport of the heat available for melting ice. In the meridional direction, the transport and its variability are dominated by the inflow in the PITW, PITE, and AC troughs (Figures 3a and 3b), and the heat enters southward into the Pine Island Bay with values above the climatological mean in February–August (Figure 3c). The climatology of the net transport in the zonal direction is
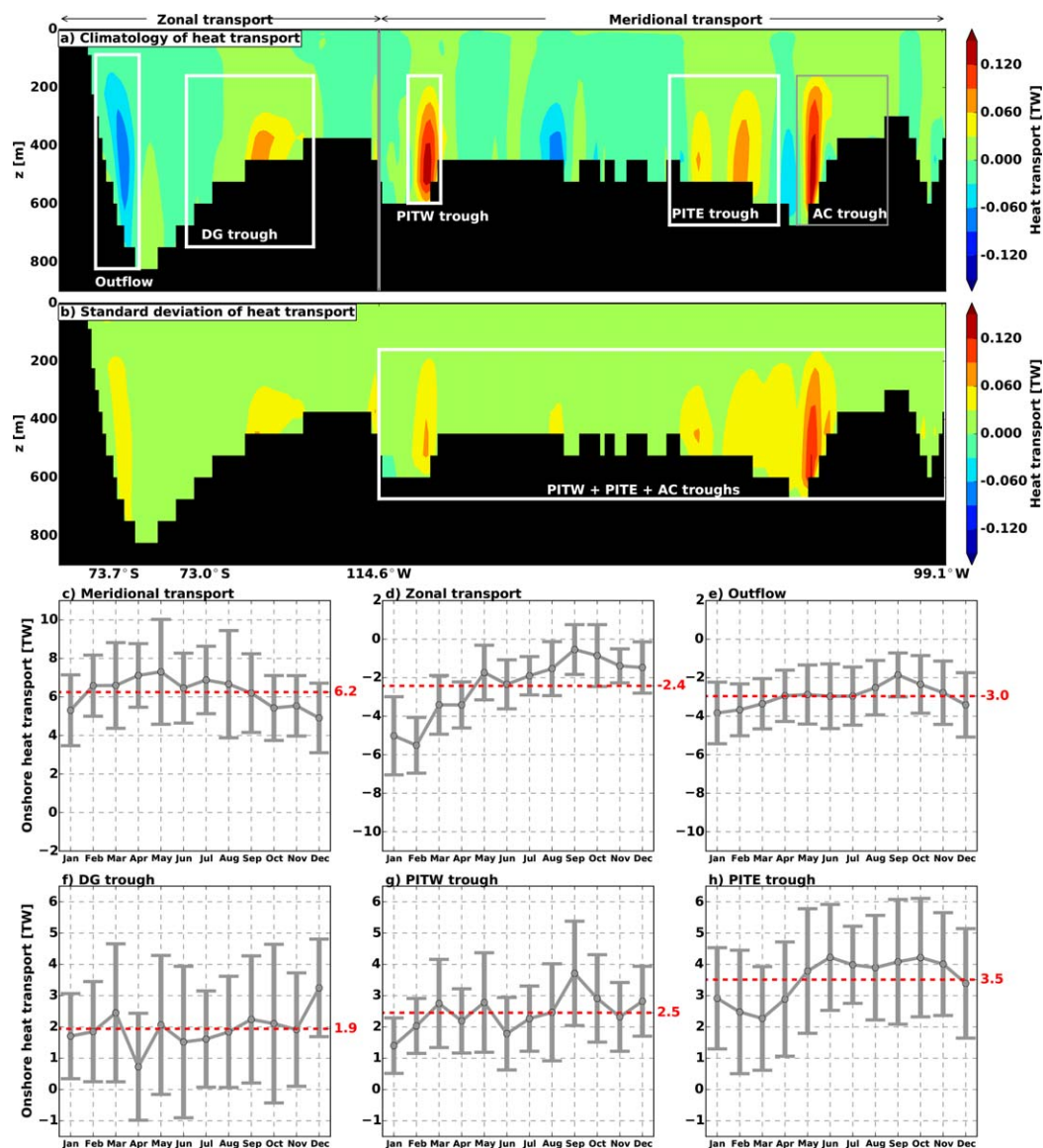

Figure 3. (a) Depth transect of climatological onshore heat transport along the western edge (zonal transport) and northern edge (meridional transport) of the green box in Figure 1. The vertical gray line indicates the boundary between the meridional and zonal directions. (b) Standard deviation of Figure 3a. (c) Seasonal cycle of depth-integrated onshore heat transport in the meridional direction in Figure 3a. (d) Seasonal cycle of depth-integrated onshore heat transport in the zonal direction in Figure 3a. (e, f) Seasonal cycle of the onshore heat transport integrated over the interior of the white boxes in Figure 3a, outflow, DG trough, PITW trough and PITE trough. The red dashed lines in Figures 3c–3h indicate the climatological mean, and the error bars indicate one standard deviation away from the seasonal mean.

negative. The net transport of -2.4 TW matches the zonal heat convergence within the box, i.e., the zonal flow underneath the Abbott ice shelf is negligible in the heat convergence in Pine Island Bay (Figure 3d). The heat is lost to the west in Pine Island Bay. The heat leaves the bay by the westward current flowing within 50 km of Dotson ice shelf, marked as "outflow" in Figure 3a. The maximum outflow occurs in January (Figure 3e). Although the net transport in the zonal direction is negative, there is a nonnegligible onshore heat transport in the DG trough (Figure 3a), which has a peak transport in December (Figure 3f).

Climatological onshore heat transports in the DG, PITW, and PITE troughs are 1.9, 2.5, and 3.5 TW, respectively (Figures 3f–3h). These transports are broadly consistent with the available observations in the area. Wåhlin et al. (2013) estimates 0.95 TW of mean onshore heat transport in the DG trough in 2010–2011 from one mooring, placed slightly west of the transect used to calculate the onshore transport in Figure 3f. The mean onshore transport in the PITW is estimated to be 2.8 ± 0.68 TW from CTD transects in 2003 (Walker et al., 2007). Our model shows that the seasonal cycle of the transport in the DG and PITW are different, despite the proximity to each other. The highest transport occurs in December (3 TW, 1.1 TW above the climatological mean) in the DG trough (Figure 3f), whereas it occurs in September (3.7 TW, 1.2 TW above the climatological mean) in the PITW trough (Figure 3g). The seasonal cycle of heat transport in the PITE trough has values above the long-term mean in May–November (Figure 3h).

The onshore heat transport in the three troughs and ice-shelf melting in Pine Island Bay have similar seasonal cycles. The seasonal cycles of melting in Cosgrove, PIG, and Thwaites have a peak melting in August–October (gray lines in Figures 4a–4c), which corresponds to the peak onshore heat transport in the PITW and PITE troughs. Peak melting of Crosson and Dotson occurs in January and February (gray lines in Figures 4d and 4e), which is one month after the peak onshore heat transport in the DG trough (Figure 3f). Melting from thinner portions of the ice shelf (ice-shelf thickness thinner than 200 m) in all the ice shelves has peak values in December–February (black lines in Figures 4a–4e). The melting of the shallow portions of the ice shelves is driven by solar heating (Figure 5a), which raises the ocean heat content in the upper 200 m (Figures 5b and 5c). The timing of the largest onshore heat transport in the DG trough is in phase with the solar heating cycle, which results in raising the surface (above 200 m) and near bottom (500–600 m) temperature in January and February at the calving front of Dotson (Figure 5b). This warming in the surface and near bottom increases the melting of Dotson in January and February. In contrast, the timing of the heat transport and the solar heating cycle is out of phase at the calving front of PIG/Thwaites, giving rise to the enhanced melting in September–November (Figure 5c). The enhanced melting in August–October in Cosgrove, PIG, and Thwaites originates from the changes in oceanic conditions at the deeper parts of Pine Island Bay, controlled by the inflow in the PITW and PITE troughs.

The seasonal cycle of Crosson melting differs from the other ice shelves. Although both Crosson and Thwaites are separated from the main trunk of DG trough by the shallow bathymetry between Dotson and Crosson, the seasonal cycle of Crosson does not match Thwaites. Instead, the seasonal cycle of Crosson matches Dotson. This difference is due to the representation of ice-shelf thickness distribution in the model. The ice-shelf thickness distribution of Crosson is flatter and thinner than Cosgrove, PIG, Thwaites, and Dotson (Figures 4f–4j), and over 80% of the water depth beneath Crosson is shallower than 200 m (Figure 4o). Crosson ice-shelf cavity is, therefore, shallower than Cosgrove, PIG, Thwaites, and Dotson ice-shelf cavities (Figures 4k–4o). The warm deep waters from the continental shelf break cannot intrude into the Crosson ice-shelf cavity, and the seasonal cycle of melting is dominated by solar heating, which results in a different seasonal cycle of melting compared to Cosgrove, PIG, and Thwaites. Even though the seasonal cycles of Dotson and Crosson are similar, the driving mechanism is different. The bathymetry in the model is derived from the RTOPO gridded data set (Timmermann et al., 2010), in which the shallow area offshore of the Crosson calving front and the ice-shelf cavities of Crosson, Dotson, and Thwaites reflect a lack of observation rather than reality. It is possible that the Crosson cavity is connected to the main Pine Island/Thwaites trough by a deeper, as yet unmapped, channel.

The seasonal cycle of the onshore heat transport is related to the wind field over the DG and PITW/PITE troughs. The heat source of the onshore transport lies in undercurrents flowing parallel to the continental shelf break. Increasing the eastward zonal wind stress results in the offshore Ekman transport, sloping the pressure gradient and barotropically strengthening the eastward flowing undercurrents. The DG trough extends toward the southeast direction, so the strengthened undercurrents directly result in increasing the onshore heat transport in December and January (Figure 6a). In contrast, the PITW and PITE troughs are
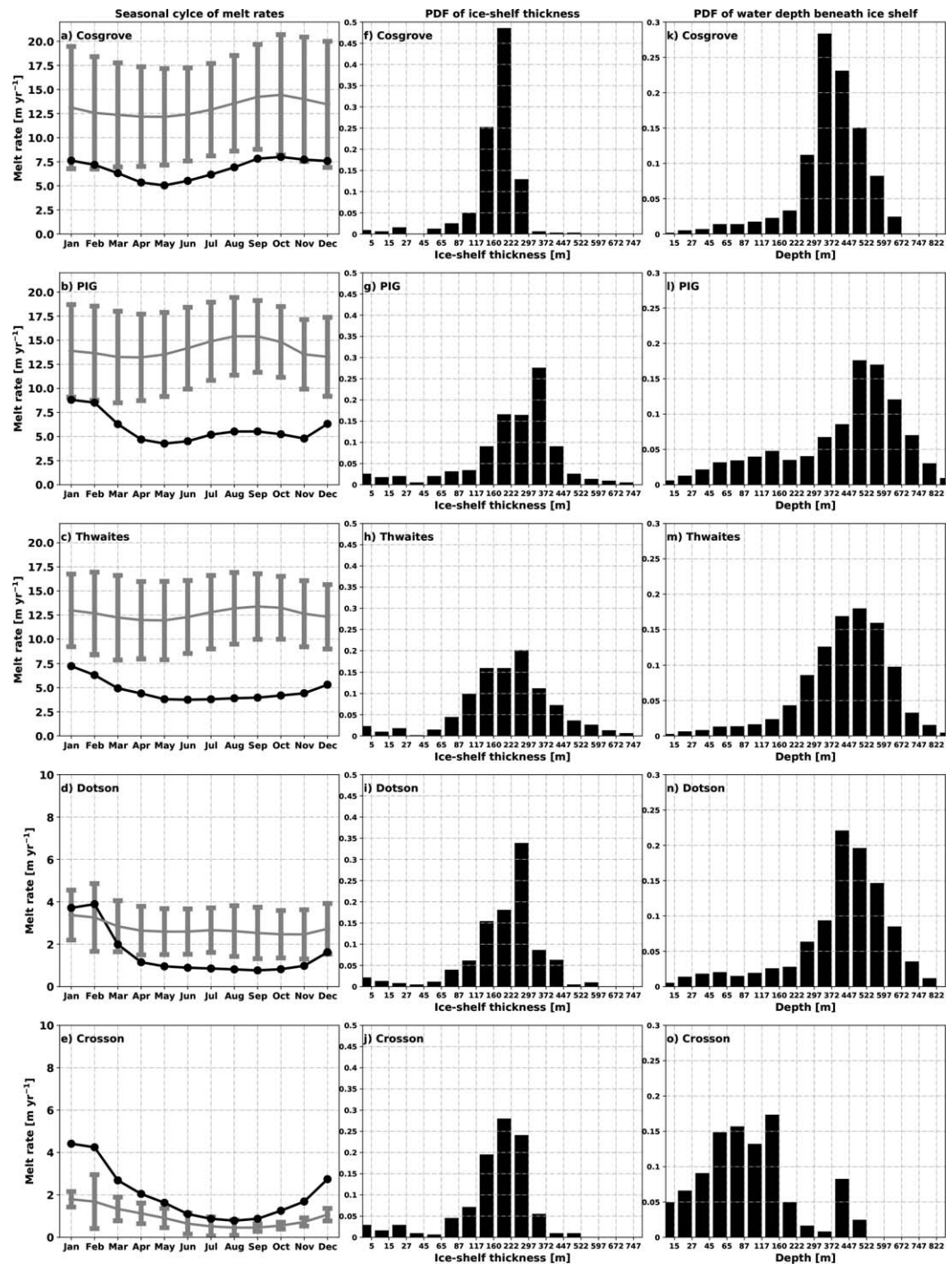
Figure 4. Seasonal cycle of melt rates in (a) Cosgrove, (b) PIG, (c) Thwaites, (d) Dotson, and (e) Crosson in the ERA-Interim simulation. The black lines indicate the melt rates of thinner parts (<200 m) of the ice shelf, and the gray lines indicate the melt rates of the entire ice shelf. The error bars indicate one standard deviation from the seasonal mean. (f–j) Probability density function (PDF) of ice-shelf thickness used in the model. (k–o) PDF of water depth beneath the ice shelf used in the model.

oriented almost meridionally, extending toward the south, so the undercurrents need to deflect southward to increase the onshore heat transport. The positive zonal wind stress and negative wind stress curl over the PITW and PITE troughs in austral winter correspond to the timing of positive onshore heat transport in the PITE trough (Figure 6b). The largest melting of PIG and Thwaites in September–November is a few
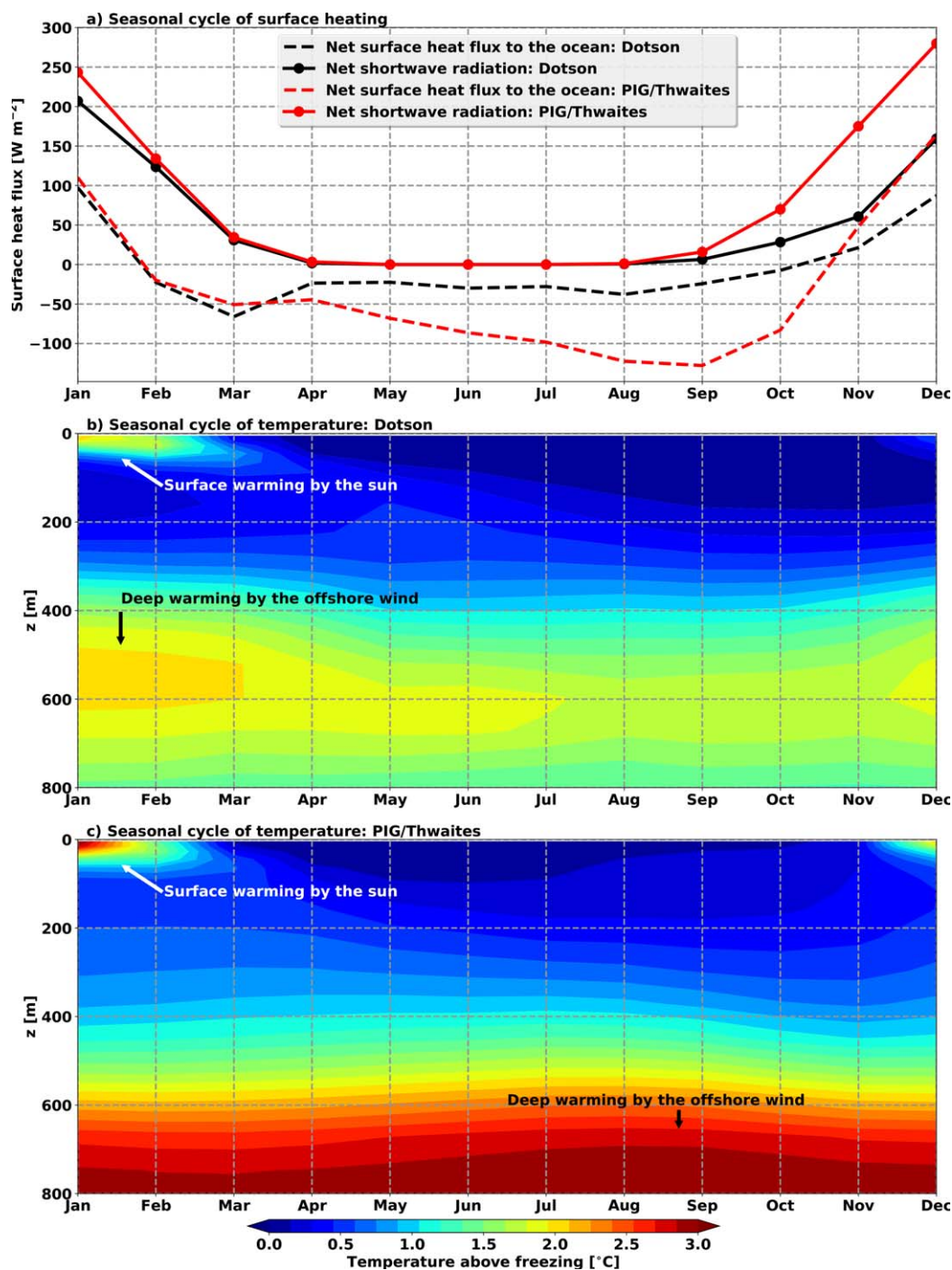
Figure 5. (a) Seasonal cycle of surface heating. (b) Seasonal cycle of the horizontally averaged temperature inside box A in Figure 1. (c) Seasonal cycle of the horizontally averaged temperature inside box B in Figure 1. All the quantities plotted come from the ERA-Interim forced simulation.

months after the peaks in the zonal wind signal. The distance between the PIG calving front and continental shelf break is about 600 km (Figure 1), and the inflow typically occurs between 400 and 600 m depth (Figure 3a). The travel time of 2 months gives the speed of 0.1 m s^{-1}, which is consistent with the climatology of inflow speed at the continental shelf break and the flow speed along the coast leading to the PIG calving front at a depth of 445 m (Figure 2a). The seasonal cycle of the transport over the continental shelf break and the zonal wind stress over the PITW/PITE troughs are broadly consistent with the analysis
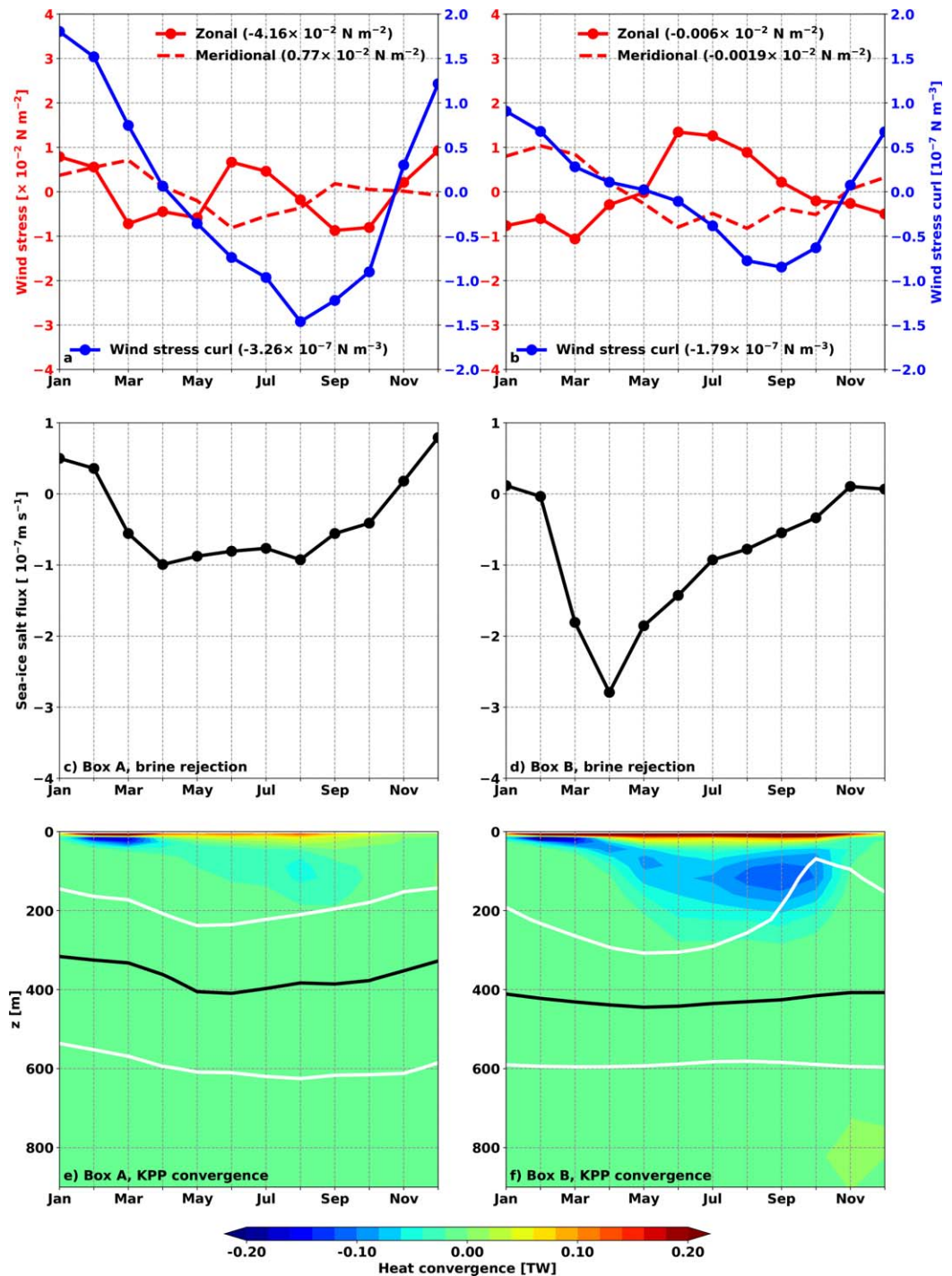
Figure 6. (a, b) Seasonal cycle of the wind field with a 3 month running mean (climatology removed) over (a) the DG trough and (b) the PITW and PITE troughs, shaded regions in Figure 1. The values inside the bracket in the legends indicate their climatological values. (c, d) Seasonal cycle of the sea-ice freshwater flux (negative for brine rejection) at the calving front of (c) Dotson and (d) PIG/Thwaites. (e, f) Seasonal cycle of the heat convergence by the KPP term at the calving front of (e) Dotson and (f) PIG/Thwaites. The contours represent the isopycnal levels of 1,027.5 (white), 1,027.6 (black), and 1,027.7 (white) kg m^{-3} from top to bottom. Seasonal cycles plotted here are derived from the ERA-Interim forced simulation.

by Steig et al. (2012), who used atmospheric reanalysis products and the ocean model outputs from Thoma et al. (2008). Steig et al. (2012) showed that the wind field over the continental shelf break was influenced by the sea surface temperature variability in the central tropical Pacific Ocean. Surface warming in the

tropics enhances atmospheric convection and generates an atmospheric Rossby wave response that influences atmospheric circulation over the Amundsen Sea (Ding et al., 2011).

Seasonal changes in brine rejection are not strong enough to influence the deep water near the calving fronts. The strongest brine rejection (negative sea-ice salt flux) occurs in April at the PIG/Thwaites calving front (Figure 6d), whereas the brine rejection at the calving front of Dotson has a smoother seasonal cycle (Figure 6c). The convective-mixing by brine rejection results in heat divergence to the atmosphere from the KPP term (a rate of change in heat due to the parameterized mixing) at the Thwaites/PIG calving front (Figures 6e and 6f). As a result, the cold surface water penetrates to the interior of the ocean, but this brine induced mixing is not strong enough to change the properties of deep waters below 300 m (Figure 6f). This implies that the seasonal cycle of surface buoyancy forcing near the calving front is not generally strong enough to cool the water entering Dotson, Thwaites and PIG ice-shelf cavities.

5. Interannual Variability

The model variability is broadly consistent with existing observations, with a larger magnitude of the variability in ERA-Interim simulation than RACMO2.3 simulation. In particular, both simulations capture the relatively warm phase during 2005–2010 and cold phase in the late 1990s, early 2000, and late 2012–2014, which are consistent with historical hydrographic measurements in Pine Island Bay (Figure 7a). Nevertheless, there are some deficiencies in the model. The deep water temperatures near the ice front in the ERA-Interim simulation from 1997 to 2001 are generally colder than what has been observed in 2000 (e.g., Dutrieux et al., 2014; Jacobs et al., 2011). The gradual cooling phase (March 2011 to December 2012) in the observations is absent in the model results. The mooring record in March 2011 to December 2012 shows a deepening of the 0.8°C isotherm from 650 to 750 m (Jenkins et al., 2016; Webber et al., 2017), whereas the ERA-Interim maintains a constant isotherm depth until October 2012 and deepens suddenly (Figure 7a). The isotherm in the RACMO2.3 simulation during this time has a deepening trend, but the depth of the isotherm is shallower than the observations. This discrepancy could be due to an inaccurate surface forcing. The gradual cooling in March 2011 to December 2012 is also absent in the simulation of St-Laurent et al. (2015), but their simulation also shows a rapid cooling in October 2012.

The cooling and warming phases are related to the propagations of temperature anomalies from the continental shelf break to the ice shelves (Figures 7b–7d). We define these anomalies as the signal with the mean seasonal cycle from 1991 to 2014 removed. The propagation of temperature anomalies from the PITW and PITE troughs controls the variability in the calving front of PIG (Figures 7b and 7c). The cold anomalies have the propagation speed of 0.02 m s^{-1}, whereas the warm anomalies propagate faster, 0.05–0.08 m s^{-1} (Figure 7c). Perhaps surprisingly, there is no obvious sign of anomaly propagation along the DG trough leading to Dotson ice shelf (Figure 7d). Instead, anomalies there seem to appear first at or near the ice-shelf front. At interannual to decadal time scales, we note however a relative coherence between the eastern (PITW and PITE) Amundsen and western (DG) Amundsen basins, with a tendency for anomalies to emerge with a few months delays on the western side. As a result, the Dotson melting lags behind the PIG melting in 2001–2006 (Figures 8d and 8f), perhaps indicative of a one-way connectivity between the basins. The continental shelf break is located closer to Dotson than to PIG, and the bathymetry does not deepen as much toward the calving front in Dotson relative to in PIG. The propagation of anomalies to the calving front of Dotson is quicker than to the calving front of PIG.

The temperature anomalies at the continental shelf break are controlled by the changes in the onshore heat transport anomalies. Temperature anomalies in the PITW trough are more negative than in the PITE trough during 2008–2011 (Figures 7b and 7c), but there are no changes in the anomalies at the calving front, suggesting that PITW has weaker links to ice front variability than PITE. This signal is repeated in the onshore heat transport anomalies, i.e., the onshore heat transport anomalies in the PITW trough are more negative than in the PITE trough during 2008–2011 (Figures 8a and 8b). The onshore heat transport anomalies have the largest variability in the DG trough with a standard deviation of 1.9 TW, followed by the PITE trough (1.8TW) and PITW trough (1.2 TW). The onshore heat transport controls the ice-shelf melting. That is, the time periods having positive heat transport anomalies correspond to positive melting anomalies (Figures 8a–8e). The variability of PIG melting (Figure 8d) corresponds well to the variability in the combined
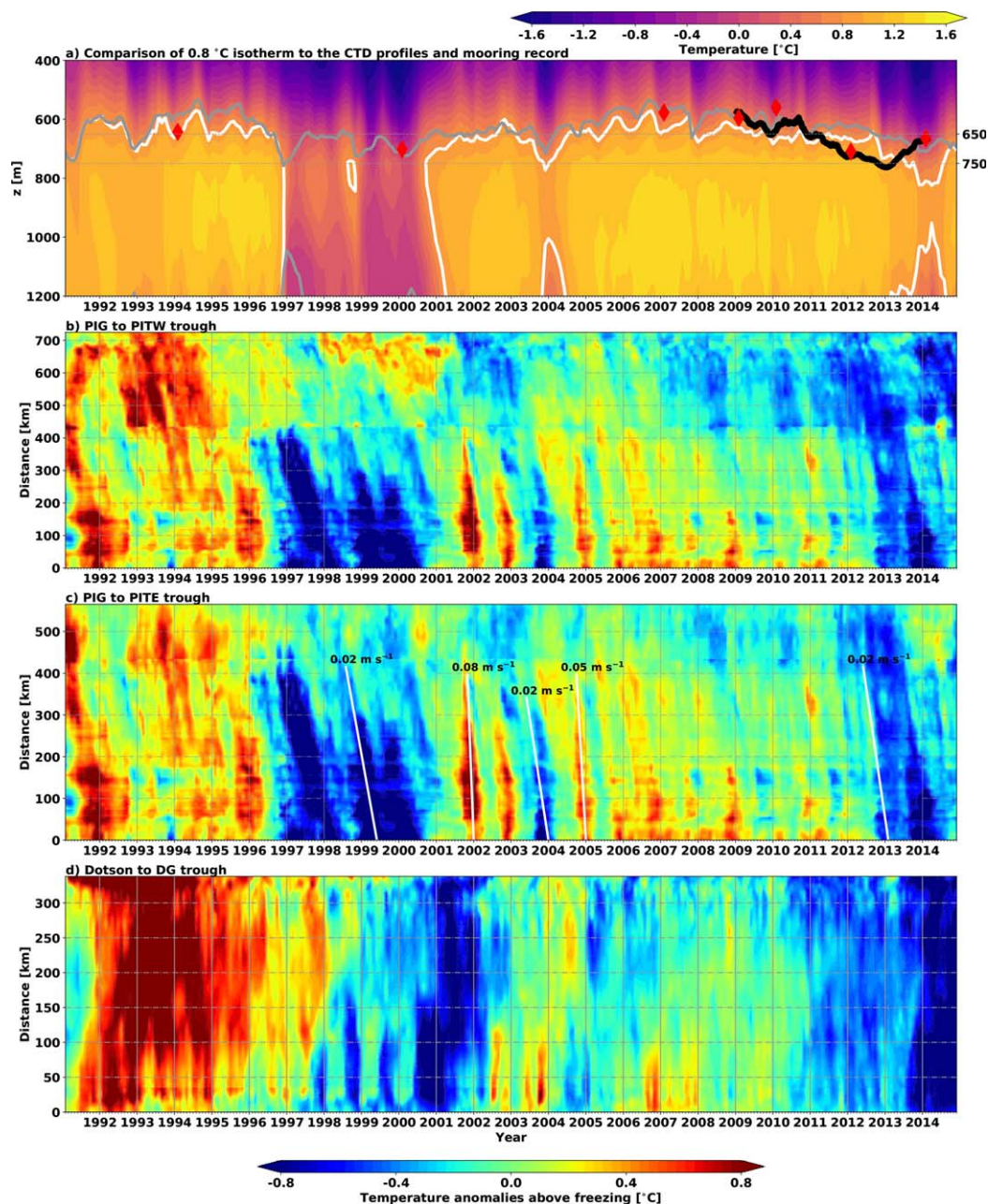
Figure 7. (a) Time series of temperature averaged over the box B in Figure 1 in the ERA-Interim simulation (color). The lines indicate the depth of 0.8°C isotherm derived from the ERA-Interim simulation (white), RACMO2.3 simulation (gray), and mooring data (black). The isotherm derived from the averages over summer CTD profiles are in red diamonds. The mooring data and CTD stations are described in Jenkins et al. (2016). (b–d) Hovmöller plots of temperature anomalies above freezing in ERA-Interim simulation at the 1,027.7 kg m^{-3} isopycnal level averaged over 10 neighboring grid points along the three red tracks in Figure 1, which lead to the (b) PITE, (c) PITW, and (d) DG troughs.

onshore heat transport in the PITW, PITE, and AC troughs (Figure 8c), where the Dotson melting is controlled by the onshore heat transport in the DG trough (Figures 8e and 8f).

The link between the ice-shelf melting and the heat transport anomalies in the troughs is assessed by the cross-correlation coefficient (*r*) of monthly melting anomalies to the monthly onshore heat transport anomalies from 1991 to 2014 (Figures 8g and 8h). The cross-correlation method is not able to distinguish the propagation speeds between warm and cold anomalies. We will discuss this separately in section 7. Although the onshore heat transport anomalies and the melting anomalies are positively correlated, the
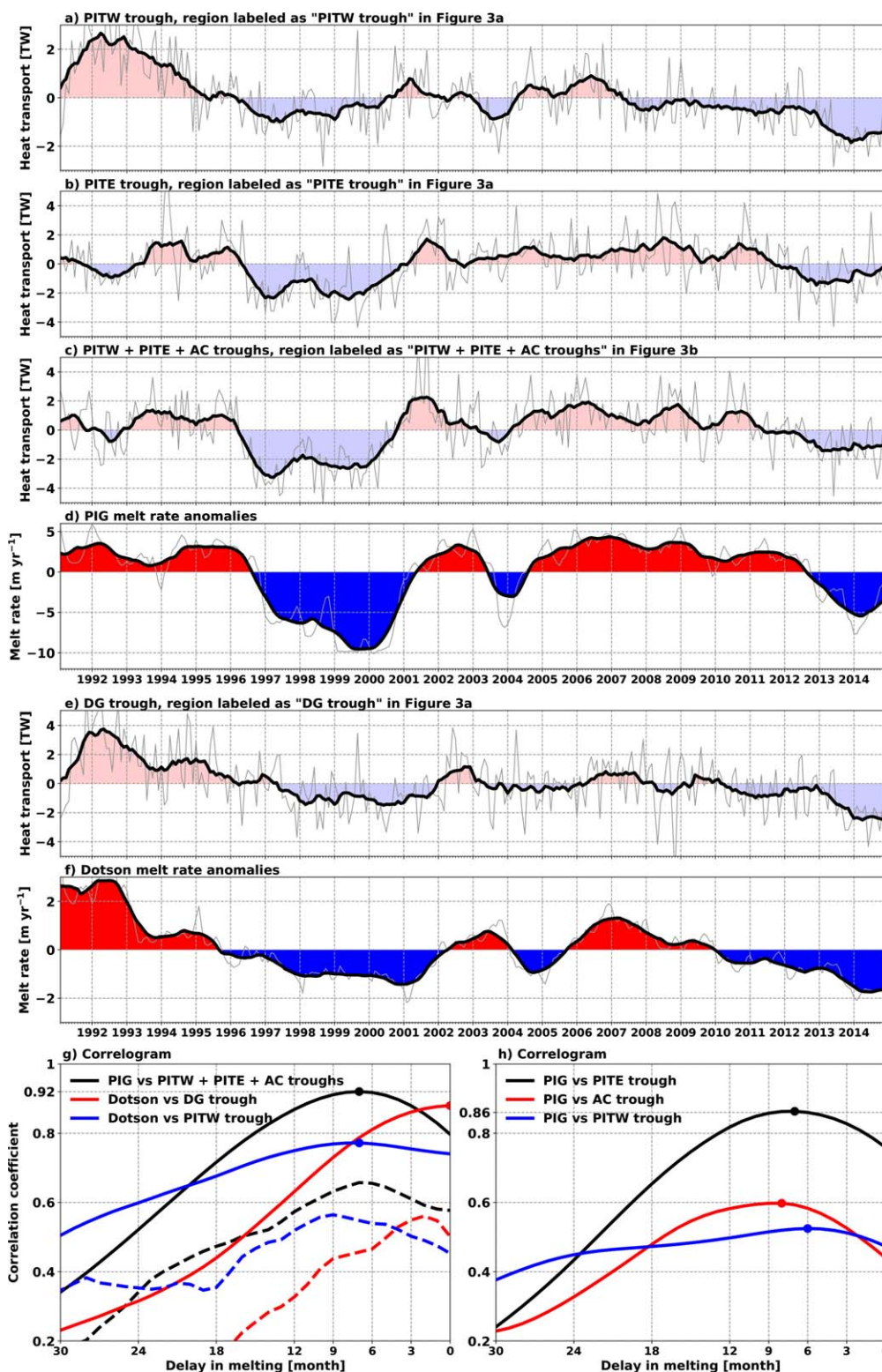
Figure 8. (a–f) Time series of the onshore heat transport anomalies and ice-shelf melt rate anomalies in ERA-Interim simulation. The thin gray lines indicate the monthly outputs, and the thick solid lines are the monthly outputs filtered with a 13 month running mean. (g–h) Correlation coefficient of the melting anomalies to the onshore heat transport anomalies versus lag. The onshore heat transport anomalies in the AC trough is defined as the transport integrated over the interior of the gray lines in Figure 3a. The dashed lines indicate the correlation calculated from the monthly time series, whereas the time series are averaged with a 13 month running mean in the solid lines.

correlation coefficient increases: (1) when the melt rate time series is shifted backward in time with respect to the onshore heat transport time series and (2) when both of the time series are averaged with a 13 month running mean. The PIG melt rate anomalies (time series in Figure 8d) have a very strong correlation ($r = 0.92$) to the combined transport anomalies in the PITW, PITE, and AC troughs (time series in Figure 8c) with a delay in melting of 7 months (Figure 8g). Among the three troughs, the PITE trough has the strongest correlation ($r = 0.86$) to the PIG melting, followed by the AC trough ($r = 0.6$) and PITW trough ($r = 0.52$) (Figure 8h). This implies that the variability in PIG ice-shelf melting comes primarily from PITE and AC troughs, where observations typically reveal the presence of warmer CDW derived waters (e.g., Jacobs et al., 2012). The lowest correlation in the PITW trough lends support to the idea that the PITW trough is not the dominant driver of interannual variability in the calving front of PIG, as suggested by the mooring record (Webber et al., 2017). The Dotson melting anomalies (time series in Figure 8f) have the strongest correlation ($r = 0.89$) to the transport anomalies in the DG trough (time series in Figure 8e) without any delays in melting, but the delay of 2 months is present when the time series are not averaged ($r = 0.56$; Figure 8g). The onshore heat transport in the PITW trough is more correlated to the melting of Dotson ($r = 0.77$) than the melting of PIG ($r = 0.52$), with a delay in melting of 7 months (Figure 8g). This suggests that the variability in the PITW trough has a larger influence on melting in Dotson than in PIG. The calving front of PIG is located over 600 km away from the PITW and PITE troughs, whereas Dotson is located closer to the DG trough (300 km). The warming or cooling signal takes longer to get to the PIG than Dotson.

6. Effects of Atmospheric Forcing

The onshore heat transport anomalies averaged with a 13 month running mean in the DG and PITE troughs have a strong correlation to the melting of Dotson and PIG, respectively. We assess how these transport anomalies are related to the atmospheric forcing. The leading hypotheses for what controls the onshore heat transport are the offshore zonal wind stress and associated wind stress curl (Dutrieux et al., 2014; Steig et al., 2012; Thoma et al., 2008); however, the wind stress is not the only source of stress acting on the sea surface in the Amundsen Sea. The prevalent sea-ice cover in the Amundsen Sea means that the combination of the wind and sea-ice motions exerts the stress on the sea surface. The effect of the sea-ice motion is substantial on the curl of stress exerted on the surface (Figures 9a and 9b). The surface stress (combination of the wind and sea-ice motions) curl has much higher regional variability than the wind stress curl alone, and the locations of negative surface stress curl coincide with the areas of strong onshore flow (Figure 9b).

To examine the spatial variation, we construct maps showing the correlation of the onshore heat transport anomalies in the DG and PITE troughs to the (1) zonal wind stress anomalies, (2) zonal surface stress anomalies, (3) wind stress curl anomalies, and (4) surface stress curl anomalies (Figures 9c–9j). The onshore heat transport in the DG trough is moderately correlated ($0.4 < r < 0.6$) to the zonal wind stress and the zonal surface stress over the area of a strong undercurrent (115°W–120°W, 72°S–72.5°S), which is the flow leading to the DG trough (Figures 9c and 9d). The same level of correlation is found in the correlation map by Wåhlin et al. (2013), which is the correlation of the flow speed in the DG trough from the mooring record to the zonal wind from ERA-Interim in March 2010 to January 2011. The correlation maps of the wind stress curl and the surface stress curl are very different. The surface stress curl over the DG trough retains a strong negative correlation ($r < -0.75$), but the correlation to the wind stress curl does not. That is, the time periods having negative stress curl anomalies correspond to positive onshore heat transport anomalies. The onshore heat transport in the PITE trough is slightly correlated ($0.2 < r < 0.4$) to the zonal wind and the zonal surface stress anomalies just north of the DG trough (Figures 9g and 9h). This lends support to the idea that the locally strengthened undercurrent north of the DG trough is linked to the variability in the onshore flow in the PITE trough. The transport in the PITE trough is strongly correlated to the local surface stress curl over the PITE trough (Figure 9j), whereas the correlation to the wind stress curl is weaker and located away from the PITE trough (Figure 9i). The surface stress curl anomalies at the longitude and latitude of 105°W and 71.7°S has the strongest negative correlation ($r = -0.8$) to the onshore heat transport anomalies in the PITE trough, and 0.3° north of this location has a moderate positive correlation ($r = 0.54$; Figure 10a).

An alternative hypothesis for what controls the melting is the modulation of ocean heat content by brine rejection as a result of coastal polynya formations near the calving front of ice shelves (negative sea-ice salt
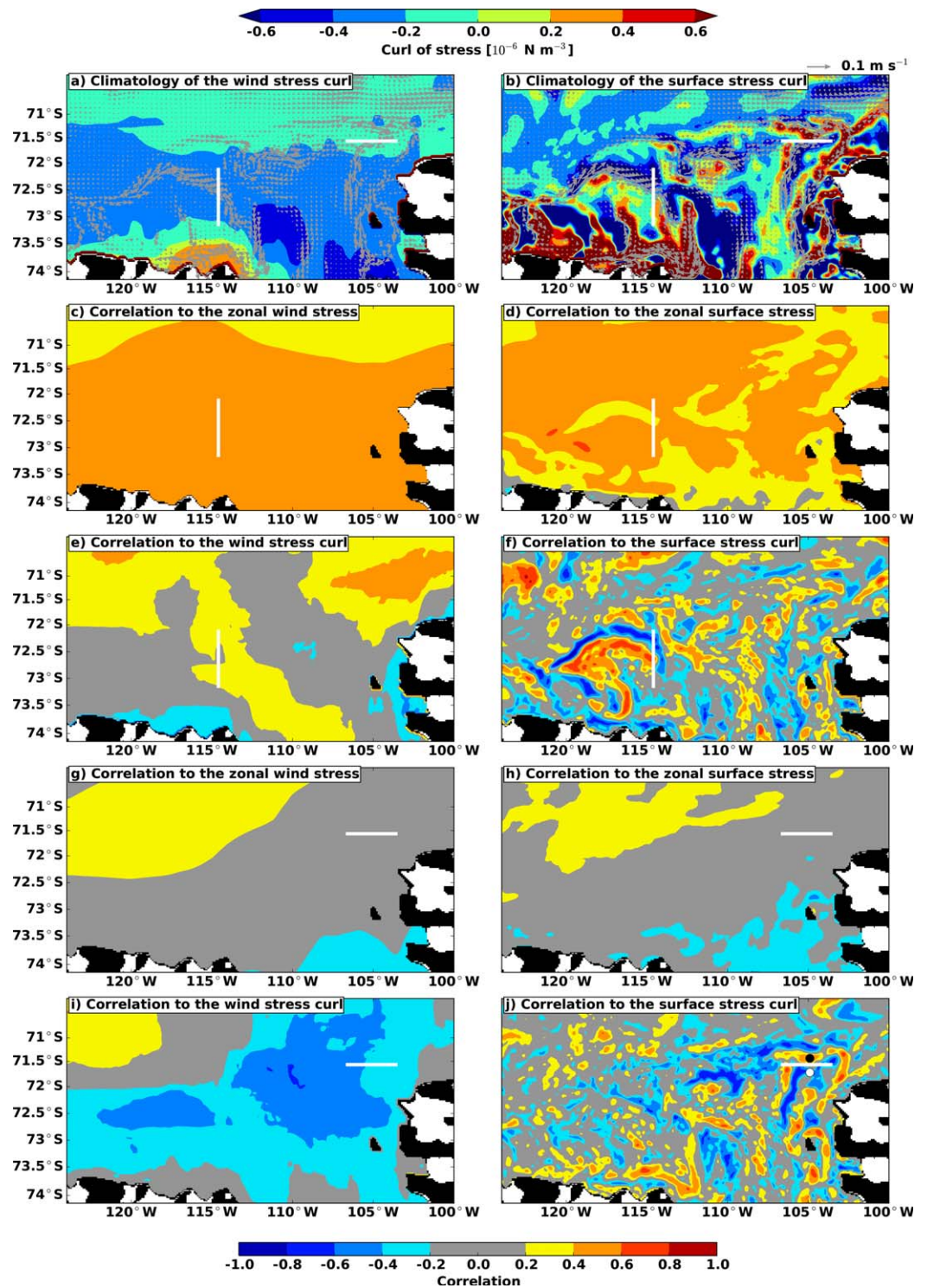
Figure 9. Climatology of (a) the wind stress curl and (b) the ocean surface stress curl in ERA-Interim simulation. The white lines indicate the DG and PITE troughs, and the arrows represent the climatological velocity vector at 447.5 m depth plotted every 3 grid points. (c–f) Correlation coefficients of the onshore heat transport in the DG trough to the wind and surface stress variables in ERA-Interim simulation. (g–j) Correlation coefficients of the onshore heat transport in the PITE trough to the surface forcing variables in ERA-Interim simulation. The gray shaded regions in Figures 9c–9j indicate the regions where the absolute value of the correlation is less than 0.2.
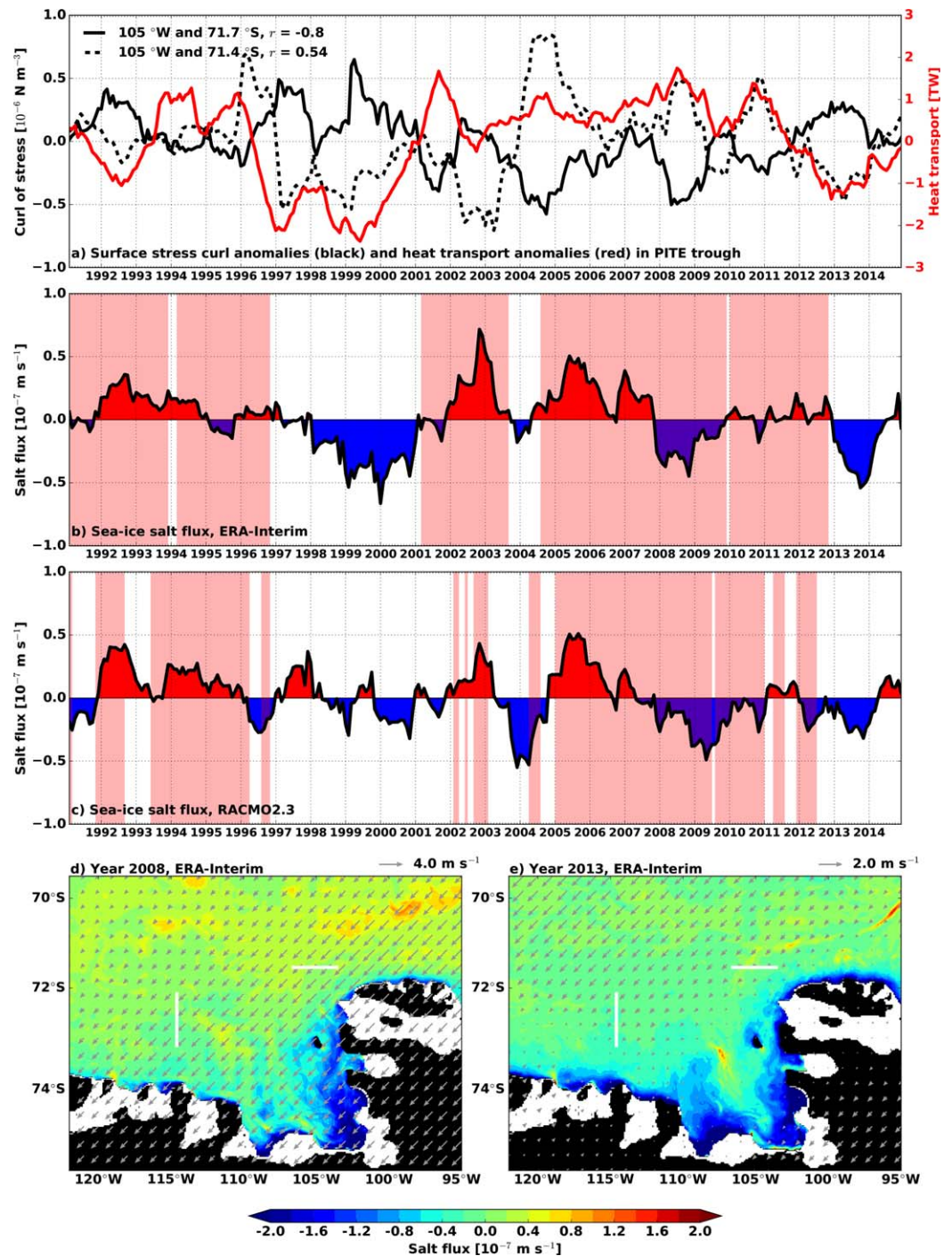
Figure 10. (a) Time series of the onshore heat transport anomalies in the PITE trough and the surface stress curl anomalies. The white dot (105°W and 71.7°S) and black dot (105°W and 71.4°S) in Figure 9j indicate the locations of the surface stress curl anomalies. Both of the time series are filtered with a 13 month running mean. (b, c) Time series of the sea-ice salt flux near the calving front of PIG and Thwaites, averaged over box B with a 13 month running mean. The light red shading regions in the background indicate the months when the PIG melt rate anomalies are positive. (d, e) Distribution of sea-ice salt flux anomalies in 2008 and 2013. The arrows indicate the anomalies of the wind vectors during the year.

flux). The role of brine rejection at the calving front in lowering the melt rates has been highlighted in Totten Glacier in Eastern Antarctica (Khazendar et al., 2013), Wilkins Ice Shelf in the Bellingshausen Sea (Padman et al., 2012), and PIG Ice Shelf (St-Laurent et al., 2015). In our simulation, the timing of brine rejection
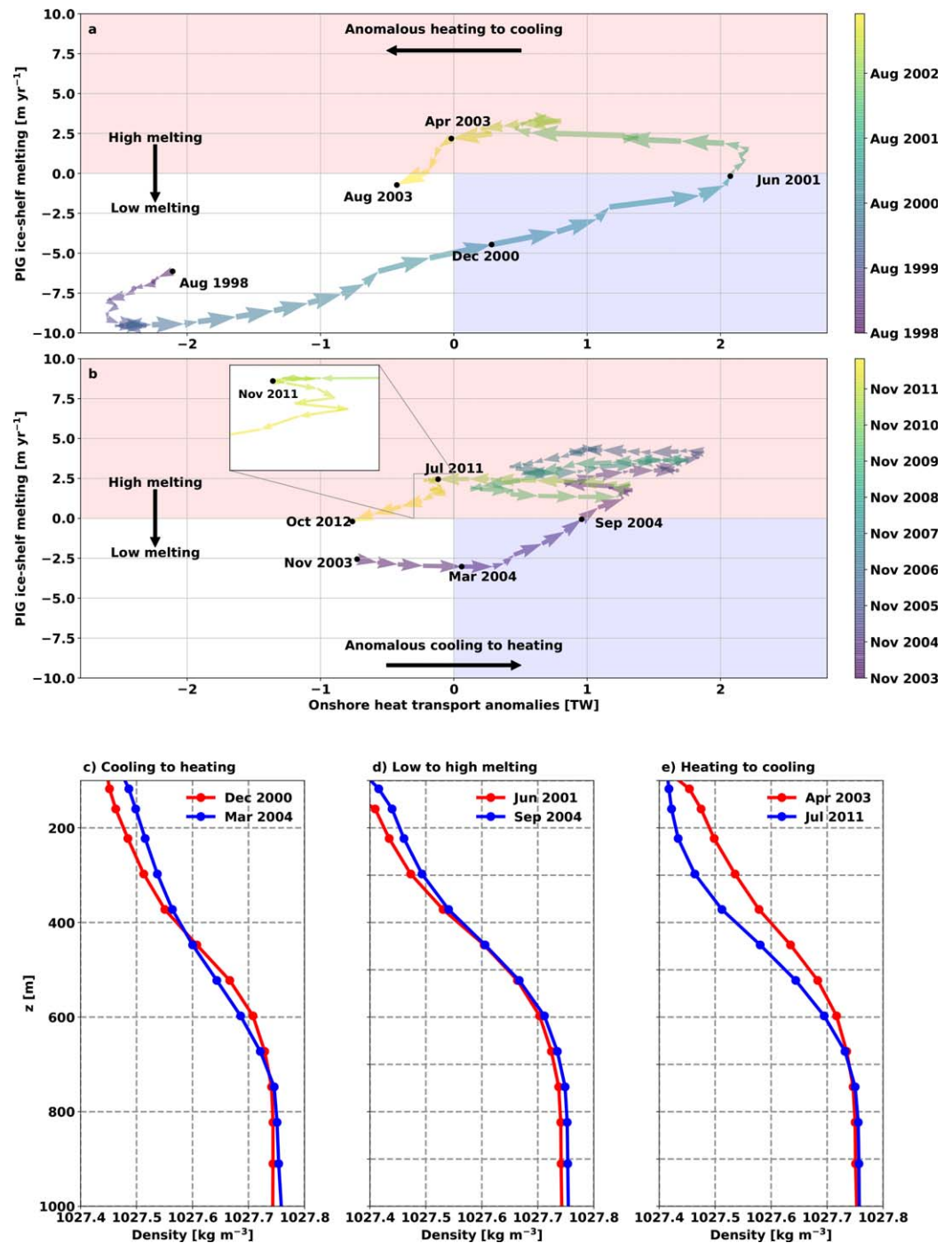
Figure 11. Phase diagram of the onshore heat transport anomalies in Figure 8c and PIG melting anomalies in Figure 8d from (a) August 1998 to August 2003 and (b) November 2003 to October 2012. Each arrows represent the state transition that occurs in 1 month. (c, d) Density profiles at the PIG calving front (box B in Figure 1) from the selected months. The selected months are indicated in Figures 11a and 11b.

(negative sea-ice salt flux anomalies) at the calving front does not coincide with the lowering of PIG melt rates (Figures 10b and 10c). The sea-ice salt flux is negative during the high ice-shelf melting years (2008–2009) as well as in the low-melting years (2013–2014; Figure 10b). In RACMO2.3 forced simulation, the sea-ice salt flux during 2008–2009 is more negative than 2013–2014, with no apparent impacts on the ice-shelf melting (Figure 10c), which contradicts with the idea that the brine rejection directly lowers the ice-shelf melting by cooling the warm deep water below the thermocline.

Brine rejection is strong along the calving front of the ice shelves, but the wind patterns over Pine Island Bay are quite different between 2008 and 2013 (Figures 10d and 10e). The northeastward wind anomalies in 2013 over Getz and Dotson ice shelves increase the brine rejection at their calving fronts, but the wind anomalies over the PITE trough are weaker compared to 2008 (Figure 10e). This results in lowering the onshore heat transport in the PITE trough in 2013 relative to 2008 (Figure 10a). In the absence of strong onshore heat transport, it may be possible for brine rejection to lower PIG melt rate (Webber et al., 2017), but brine rejection alone appears to be insufficient to explain the interannual variability in PIG melting. In our simulations, the reduction of onshore heat transport likely weakens the stratification at the calving front, enables the sea-ice formation to deepens the surface mixed layer and leads to further reduction in ice-shelf melting.

7. Discussion

Although the combined onshore heat transport in the PITW, PITE, and AC troughs has the strongest correlation to the PIG melt rate anomalies, PIG melt rate responds asymmetrically to changes in ocean heat transport; melting responds more rapidly to increases in ocean heat transport than decreases in ocean heat
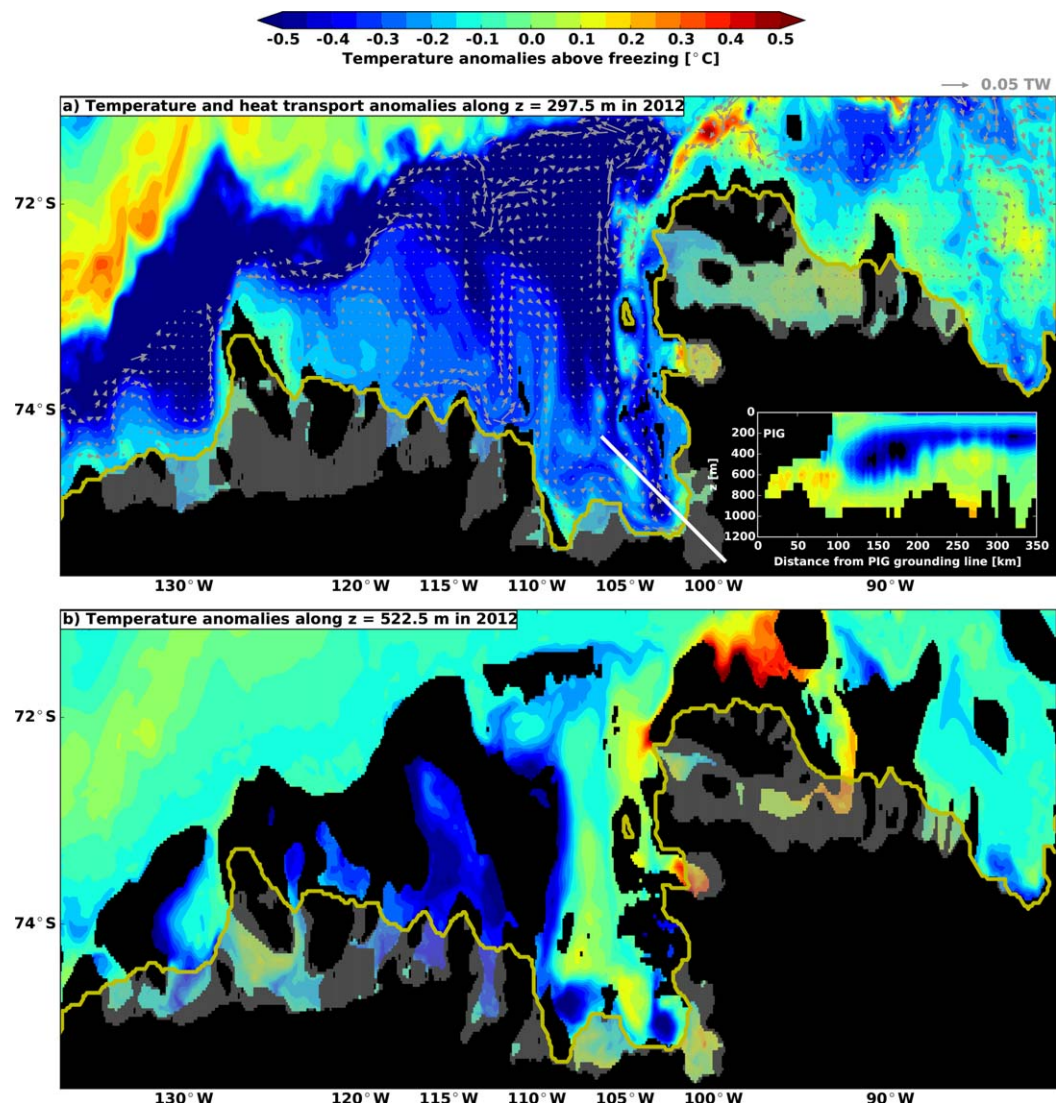

Figure 12. Anomalies of temperature (color) and heat transport (arrows) in 2012 from (a) z = 297.5 m and (b) z = 522.5 m. The white line in Figure 12a indicates the depth section plotted in the bottom right.

transport. The arrows in the phase diagram (Figures 11a and 11b) are steeper in the direction of positive heat transport than negative heat transport. The steepness of the arrows would have been identical if the response was symmetric. When anomalies in heat transport shift from cooling to heating, anomalies in melt respond instantly (for example, in the blue shaded regions in Figures 11a and 11b). In contrast, melting anomalies do not respond immediately in the phase of decreasing heat transport anomalies. The melting anomalies do not change for a long period of time, before they fall suddenly in April 2003 and November 2011 (red shaded regions in Figures 11a and 11b).

More generally, the transition from low melting to high melting occurs in 6 months after the anomalies in heat transport shift from cooling to heating (December 2000 to June 2001 and March 2004 to September 2004). In contrast, the transition from high to low melting is delayed by 4 months (April 2003 to August 2003) and 15 months (July 2011 to October 2012). The difference in the time scale of delay is sensitive to the density profile at the calving front (Figures 11c–11e). The onshore heat transport anomalies shift from cooling to heating in December 2000 and March 2004, and the density profiles are similar during these times (Figure 11c). Increasing the onshore heat transport results in sharpening the density gradient at the calving front, eventually shifting the melting anomalies from low to high in June 2001 and September 2004 (Figure 11d). After June 2001, the anomalous heating only lasts 21 months, while it lasts 81 months after
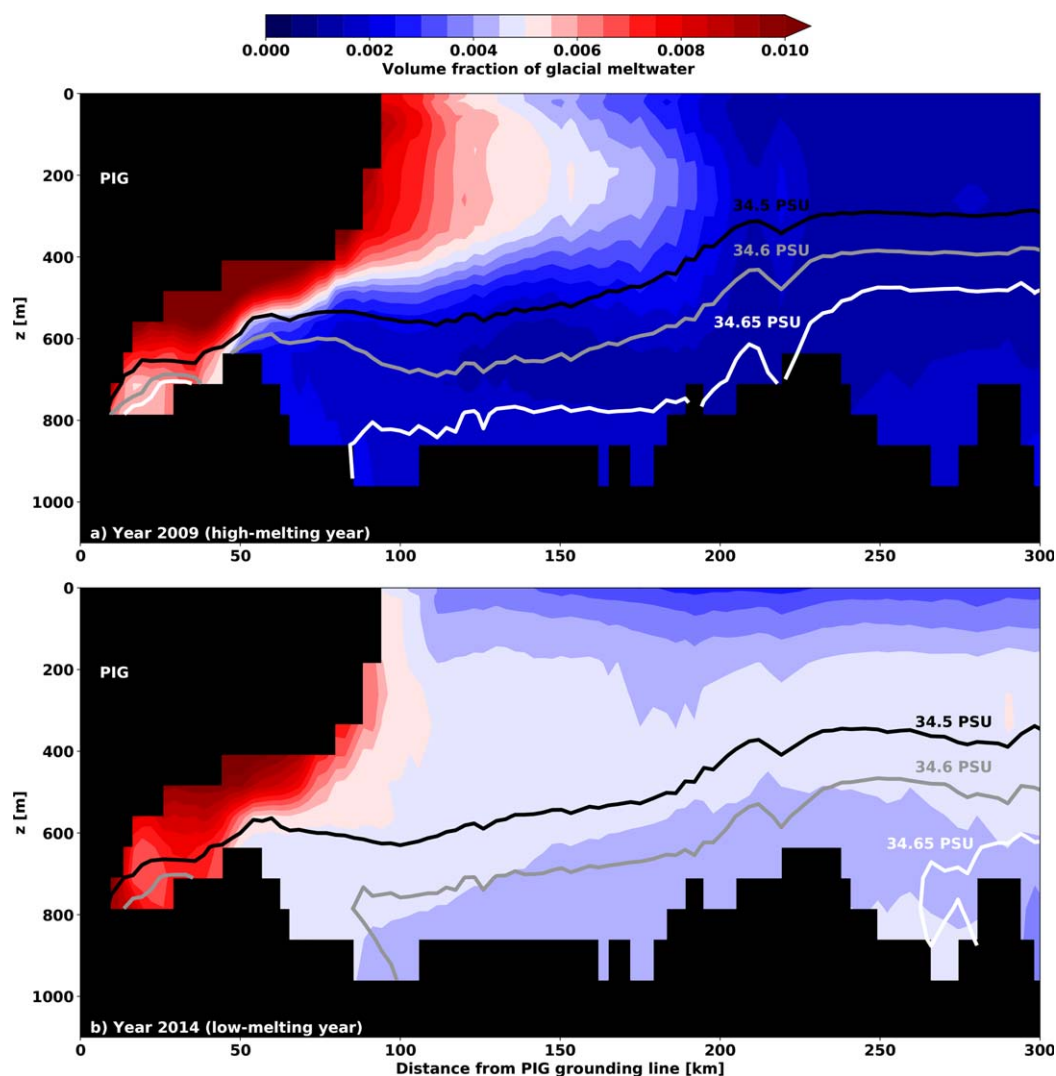

Figure 13. Difference in the circulation of glacial meltwater between high-melting and low-melting years. Volume fraction of glacial meltwater inside and outside the PIG ice-shelf cavity from (a) 2009 and (b) 2014 along the depth section indicated by the white line in Figure 12a.

September 2004. The sustained anomalous heating period of 81 months results in a sharper density gradient in July 2011 than in April 2003 (Figure 11e). This means that the stratification in July 2011 takes a longer time to erode and contains more heat at the depth near the calving front than in April 2003. The remaining heat from the recent anomalous heating phase results in sustaining the positive ice-shelf melting anomalies for 15 months (July 2011 to October 2012). Indeed, the heat is stored at the depth of thermocline in 2012, even though the onshore heat transport in 2012 is negative. The negative onshore heat transport in 2012 results in cooling along the depth of PIG ice-shelf draft, $z = 297.5$ m (Figure 12a); however, this cooling does not take place in the deeper part of the bay, $z = 522.5$ m (Figure 12b).

The circulation of glacial meltwater during high-melting phase favors the storage of heat in the deeper part of the bay, because the glacial meltwater does not contribute as much to the deep water freshening during the high-melting phase compared to the low-melting phase. During the high-melting phase, the warm, salty water from the continental shelf break infiltrates Pine Island Bay. The inland deepening of the bathymetry in the bay and beneath the ice shelf facilitates the pooling of this warm, salty water. In addition, the glacial meltwater outflow from the sub-ice-shelf cavity is more able to reach the surface, owing to the high
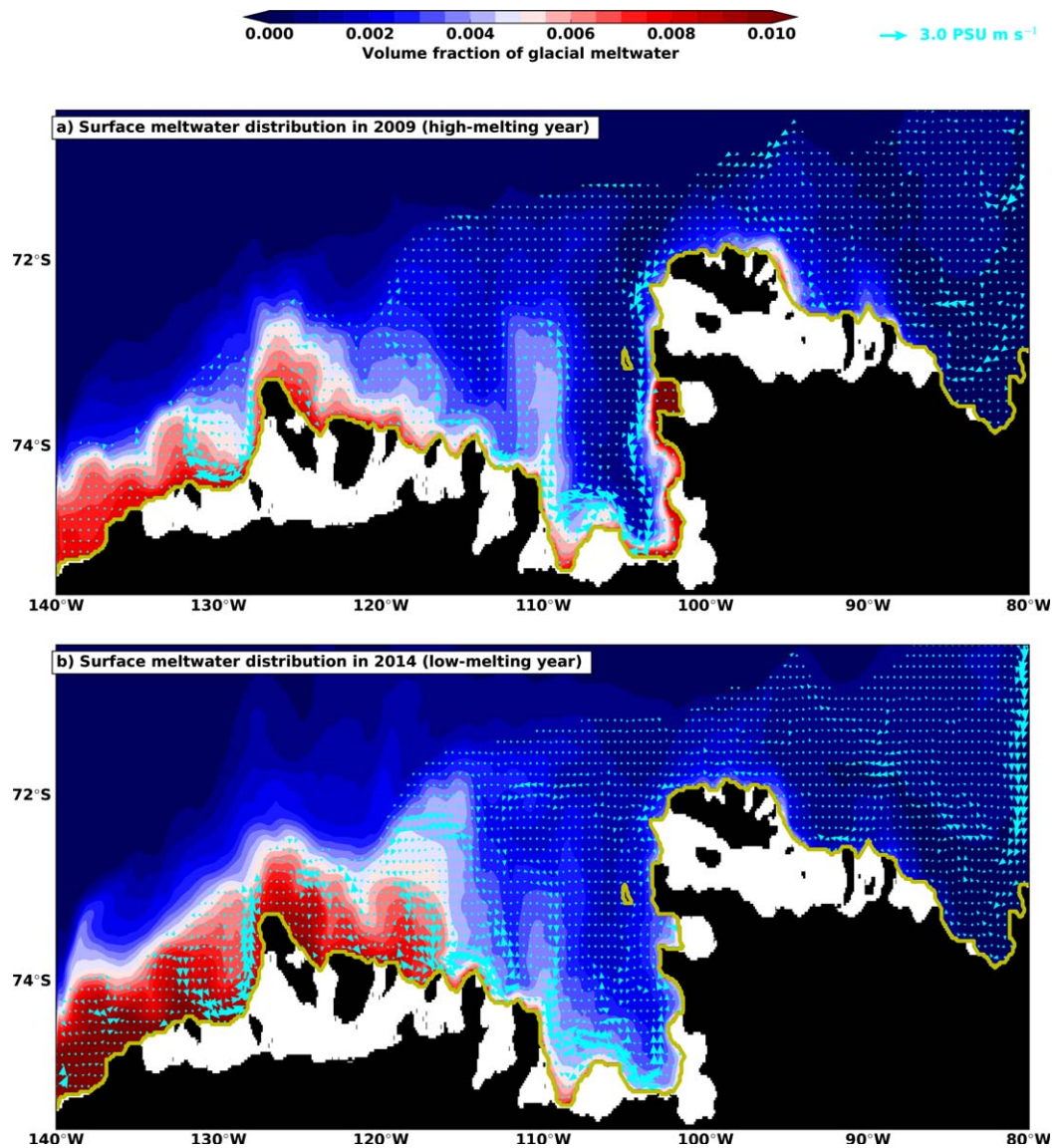

Figure 14. Surface distribution of the glacial meltwater in (a) 2009 and (b) 2014. Arrows represent salt transport anomalies plotted every four grid points.

melting, and the freshening occurs near the surface (Figure 13a). In the low-melting year, the glacial melt-water outflow retains less buoyancy, so the meltwater settles along deeper isopycnals and penetrates away from the calving front, favoring the deep water freshening (200–600 m depth in Figure 13b). This implies that the heat and salt content of the deep water is maintained more efficiently during the high-melting phase (e.g., in 2009) than the low-melting phase (e.g., 2014). This stored heat during the high-melting phase permits positive melting anomalies in the absence of onshore heat transport (e.g., in 2012). The penetration of the glacial meltwater along deep isopycnal levels and reduced onshore salt transport during the low-melting phase weaken the stratification inside the ice-shelf cavity and the calving front. The weakening of the stratification allows a rapid cascading of the denser warm, salty water flowing along the bathymetric slope from the continental shelf break to the calving front at the onset of an anomalous heating phase. This results in a shorter transition time to achieve the high-melting phase than the low-melting phase, giving rise to the asymmetric response in PIG melting. The asymmetric response in PIG melting is present in our limited model record. We do not have many state transitions to confirm that if the asymmetric response is a persistent feature in Pine Island Bay.
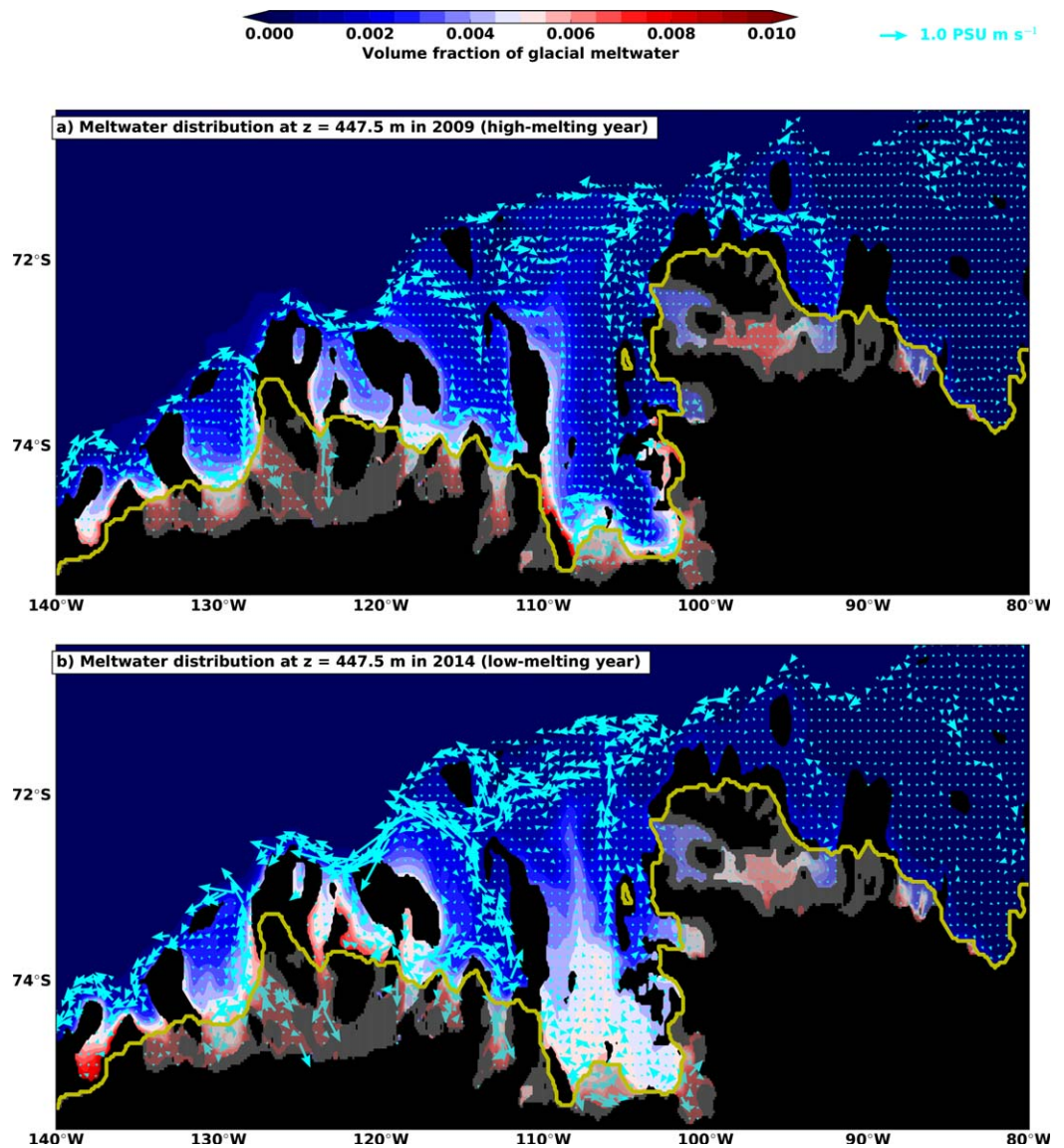

Figure 15. Horizontal distribution of the glacial meltwater at the depth of 475.5 m in (a) 2009 and (b) 2014. Arrows represent salt transport anomalies plotted every four grid points.

Upwelling of the glacial meltwater during the high-melting phase increases the horizontal density gradient near the calving front and strengthens the westward flow of the glacial meltwater at the surface, arresting the meltwater distribution within 100 km from the PIG calving front (Figure 14a). The strong westward flow and the surface freshening at the calving front will (1) contribute to the freshening of the basin west of the Amundsen Sea Embayment, such as the Ross Gyre, where a significant freshening in the past 40 years is observed (Jacobs & Giulivi, 2010) and (2) raise local sea level around the Antarctic continent by steric adjustment (Rye et al., 2014). In the low-melting phase, the westward circulation weakens (Figure 14b), and the glacial meltwater penetrates away from the calving front along deeper isopycnals relative to the high-melting phase (Figures 15a and 15b). This is consistent with the observation of meltwater more than 300 km away from the calving front of Dotson ice shelf in 2014 (Kim et al., 2016).

Any change in melt rates of ice shelves has a significant impact on the circulation of glacial meltwater in the Amundsen Sea Embayment. Our model shows that the pattern of freshening changes in a matter of a few years. This has an important implication to our interpretations of climate models. Climate models have shown that freshwater runoff from Antarctica plays a significant role in shaping the stratification and changing global heat content of the ocean (Green & Schmittner, 2015; Pauling et al., 2016; Stammer, 2008), but these models prescribe a steady surface freshwater flux at a fixed depth along the coastline. Our results demonstrate that prescribing a steady freshwater flux at any fixed depth would not (1) mimic the decadal variability of glacial meltwater discharge from ice-shelf melting and (2) permit the asymmetric response of the ice-shelf melting to the changes in the onshore heat transport.

8. Conclusions

We have investigated the variability of ice-shelf melting and oceanic conditions in the Amundsen Sea using a general circulation model with static ice shelves forced with two atmospheric forcing conditions, ERA-Interim and RACMO2.3. The model study has focused on quantifying the origin of ice-shelf melting anomalies by variability in ocean circulation. Our main findings are as follows:

1. The seasonal cycles of Cosgrove, PIG, and Thwaites melting show peak melting in August–October, whereas the peak melting occurs in January and February in Crosson and Dotson. Melting from thinner portions (<200 m) of the ice shelves have a peak melting in December–January, which corresponds to the timing of surface warming by shortwave radiation.
2. The enhanced melting of PIG and Thwaites in August–October corresponds to the seasonal cycle of the zonal wind stress and wind stress curl over the continental shelf break over the PITW and PITE troughs. This peak melting occurs even though the surface mixed layer deepens during this time due to brine rejection at the calving front. The deepening of the mixed layer is shallower than the draft of the ice shelves, and therefore the brine rejection does not control the heat content entering the ice-shelf cavities on a mean seasonal cycle.
3. The time periods having positive onshore heat transport anomalies correspond to positive ice-shelf melting anomalies. The correlation coefficient increases when both of the time series are averaged with a 13 month running mean. The PIG melting is most correlated ($r = 0.92$) to the deep onshore heat transport, which covers the PITW, PITE, and AC troughs, with a 7 month delay in melting. Out of these three troughs, the PITE trough has the strongest correlation ($r = 0.86$) followed by the AC trough ($r = 0.6$) and the PITW trough ($r = 0.52$). The anomalies in Dotson melting have a very strong correlation to the onshore heat transport anomalies in the DG trough ($r = 0.89$) without lags in melting. The transport in the PITW trough is more correlated to Dotson ($r = 0.77$) than to PIG ($r = 0.52$), suggesting a potential importance of the PITW variability in Dotson melting.
4. Changes in the onshore heat transport in the DG and PITE troughs are sensitive to the wind stress and surface stress (combined stress exerted by the wind and sea-ice motion). In general, regions of strong correlation to the zonal wind stress and zonal surface stress are located over the continental shelf break, whereas correlation to the curl has much higher regional variability. The onshore heat transport in the DG trough is positively correlated to the zonal wind, zonal surface stress and surface stress curl but not to the wind stress curl. The onshore heat transport in the PITE trough has the strongest negative correlation to the local surface stress curl.

5. The PIG melt rate responds asymmetrically to changes in ocean heat transport; the melting responds more rapidly to increases in ocean heat transport than decreases in ocean heat transport. This asymmetric response enhances PIG ice-shelf melting. The melting persists during periods of anomalously low ocean heat transport because of the heat stored in Pine Island Bay during the previous period of high melting. During the high-melting phase, the upwelling of the glacial meltwater outflow does not freshen the water at the deeper parts of the bay, favoring the heat storage.

6. A high volume of glacial meltwater along the calving front sets up a strong westward baroclinic current, arresting the distribution of glacial meltwater along shallow isopycnal levels during the high melting phase. The westward current weakens in the low-melting phase, and the meltwater penetrates further away from the calving front along deeper isopycnal levels.

7. While we do not resolve the variability of the global ocean, the effects of global atmospheric conditions on the local wind fields are represented in the model by the boundary conditions. Ocean-driven melting and resulting glacial meltwater circulation are linked to the undercurrents along the continental shelf break, wind fields and sea-ice motions at the continental shelf break.

References

Adcroft, A., Hill, C., & Marshall, J. (1997). Representation of topography by shaved cells in a height coordinate ocean model. *Monthly Weather Review*, *125*(9), 269–284.

Alley, K. E., Scambos, T. A., Siegfried, M. R., & Fricker, H. A. (2016). Impacts of warm water on antarctic ice shelf stability through basal channel formation. *Nature Geoscience*, *9*(4), 290–293.

Arndt, J. E., Schenke, H. W., Jakobsson, M., Nitsche, F. O., Buys, G., Goleby, B., . . . Wigley, R. (2013). The international bathymetric chart of the Southern Ocean (IBCSO) version 1.0—A new bathymetric compilation covering circum-antarctic waters. *Geophysical Research Letters*, *40*, 3111–3117. https://doi.org/10.1002/grl.50413

Assmann, K. M., Jenkins, A., Shoosmith, D. R., Walker, D. P., Jacobs, S. S., & Nicholls, K. W. (2013). Variability of Circumpolar Deep Water transport onto the Amundsen Sea Continental shelf through a shelf break trough. *Journal of Geophysical Research: Oceans*, *118*, 6603–6620. https://doi.org/10.1002/2013JC008871

Bracegirdle, T. J., & Marshall, G. J. (2012). The reliability of antarctic tropospheric pressure and temperature in the latest global reanalyses. *Journal of Climate*, *25*(20), 7138–7146. https://doi.org/10.1175/JCLI-D-11-00685.1

Dee, D. P., Uppala, S. M., Simmons, A. J., Berrisford, P., Poli, P., Kobayashi, S., . . . Vitart, F. (2011). The ERA-Interim reanalysis: Configuration and performance of the data assimilation system. *Quarterly Journal of the Royal Meteorological Society*, *137*(656), 553–597. https://doi.org/10.1002/qj.828

Depoorter, M. A., Bamber, J. L., Griggs, J. A., Lenaerts, J. T. M., Ligtenberg, S. R. M., van den Broeke, M. R., & Moholdt, G. (2013). Calving fluxes and basal melt rates of Antarctic ice shelves. *Nature*, *502*(7469), 89–92.

De Rydt, J., Holland, P. R., Dutrieux, P., & Jenkins, A. (2014). Geometric and oceanographic controls on melting beneath Pine Island Glacier. *Journal of Geophysical Research: Oceans*, *119*, 2420–2438. https://doi.org/10.1002/2013JC009513

Ding, Q., Steig, E. J., Battisti, D. S., & Kuttel, M. (2011). Winter warming in West Antarctica caused by central tropical Pacific warming. *Nature Geoscience*, *4*(6), 398–403.

Dutrieux, P., De Rydt, J., Jenkins, A., Holland, P. R., Ha, H. K., Lee, S. H., . . . Schröder, M. (2014). Strong sensitivity of Pine Island ice-shelf melting to climatic variability. *Science*, *343*(6167), 174–178.

Dutrieux, P., Vaughan, D. G., Corr, H. F. J., Jenkins, A., Holland, P. R., Joughin, I., & Fleming, A. H. (2013). Pine Island Glacier ice shelf melt distributed at kilometre scales. *The Cryosphere*, *7*(5), 1543–1555. https://doi.org/10.5194/tc-7-1543-2013

Favier, L., Durand, G., Cornford, S. L., Gudmundsson, G. H., Gagliardini, O., Gillet-Chaulet, F., . . . Le Brocq, A. M. (2014). Retreat of Pine Island Glacier controlled by marine ice-sheet instability. *Nature Climate Change*, *4*(2), 117–121.

Fretwell, P., Pritchard, H. D., Vaughan, D. G., Bamber, J. L., Barrand, N. E., Bell, R., . . . Zirizzotti, A. (2013). Bedmap2: Improved ice bed, surface and thickness datasets for Antarctica. *The Cryosphere*, *7*(1), 375–393. https://doi.org/10.5194/tc-7-375-2013

Gladish, C. V., Holland, D. M., Holland, P. R., & Price, S. F. (2012). Ice-shelf basal channels in a coupled ice/ocean model. *Journal of Glaciology*, *58*(212), 1227–1244.

Green, J. A. M., & Schmittner, A. (2015). Climatic consequences of a Pine Island Glacier collapse. *Journal of Climate*, *28*(23), 9221–9234. https://doi.org/10.1175/JCLI-D-15-0110.1

Gudmundsson, G. H. (2013). Ice-shelf buttressing and the stability of marine ice sheets. *The Cryosphere*, *7*(2), 647–655. https://doi.org/10.5194/tc-7-647-2013

Holland, P. R., Bruneau, N., Enright, C., Losch, M., Kurtz, N. T., & Kwok, R. (2014). Modeled trends in Antarctic Sea ice thickness. *Journal of Climate*, *27*(10), 3784–3801. https://doi.org/10.1175/JCLI-D-13-00301.1

Holland, P. R., Jenkins, A., & Holland, D. M. (2008). The response of ice shelf basal melting to variations in ocean temperature. *Journal of Climate*, *21*(11), 2558–2572. https://doi.org/10.1175/2007JCLI1909.1

Jacobs, S., Giulivi, C., Dutrieux, P., Rignot, E., Nitsche, F., & Mouginot, J. (2013). Getz ice shelf melting response to changes in ocean forcing. *Journal of Geophysical Research: Oceans*, *118*, 4152–4168. https://doi.org/10.1002/jgrc.20298

Jacobs, S., Jenkins, A., Hellmer, H. H., Giulivi, C., Nitsche, F., Huber, B., & Guerrero, R. (2012). The Amundsen Sea and the Antarctic ice sheet. *Oceanography*, *25*, 154–163.

Jacobs, S. S., & Giulivi, C. F. (2010). Large multidecadal salinity trends near the Pacific–Antarctic continental margin. *Journal of Climate*, *23*(17), 4508–4524. https://doi.org/10.1175/2010JCLI3284.1

Jacobs, S. S., Giulivi, C. F., & Mele, P. A. (2002). Freshening of the Ross Sea during the late 20th century. *Science*, *297*(5580), 386–389. https://doi.org/10.1126/science.1069574

Jacobs, S. S., Helmer, H. H., & Jenkins, A. (1996). Antarctic ice sheet melting in the Southeast Pacific. *Geophysical Research Letters*, *23*, 957–960.

Jacobs, S. S., Jenkins, A., Giulivi, C. F., & Dutrieux, P. (2011). Stronger ocean circulation and increased melting under Pine Island Glacier ice shelf. *Nature Geoscience*, *4*(8), 519–523.

Jenkins, A., Dutrieux, P., Jacobs, S., McPhail, S., Perrett, J., Webb, A., & White, D. (2010). Observations beneath Pine Island Glacier in West Antarctica and implications for its retreat. *Nature Geoscience*, *3*, 468–472.

Jenkins, A., Dutrieux, P., Jacobs, S., Steig, E. J., Gudmundsson, G. H., Smith, J., & Heywood, K. J. (2016). Decadal ocean forcing and Antarctic ice sheet response: Lessons from the Amundsen Sea. *Oceanography*, *29*(4), 106–117.

Joughin, I., Smith, B. E., & Medley, B. (2014). Marine ice sheet collapse potentially under way for the Thwaites Glacier Basin, West Antarctica. *Science*, *344*(6185), 735–738.

Jourdain, N. C., Mathiot, P., Merino, N., Durand, G., Le Sommer, J., Spence, P., . . . Madec, G. (2017). Ocean circulation and sea-ice thinning induced by melting ice shelves in the Amundsen Sea. *Journal of Geophysical Research: Oceans*, *122*, 2550–2573. https://doi.org/10.1002/2016JC012509

Khazendar, A., Schodlok, M. P., Fenty, I., Ligtenberg, S. R. M., Rignot, E., & van den Broeke, M. R. (2013). Observed thinning of Totten Glacier is linked to coastal polynya variability. *Nature Communications*, *4*, 2857.

Kim, I., Hahm, D., Rhee, T. S., Kim, T. W., Kim, C.-S., & Lee, S. (2016). The distribution of glacial meltwater in the Amundsen Sea, Antarctica, revealed by dissolved helium and neon. *Journal of Geophysical Research: Oceans*, *121*, 1654–1666. https://doi.org/10.1002/2015JC011211

Large, W. G., McWilliams, J. C., & Doney, S. C. (1994). Oceanic vertical mixing: A review and a model with a nonlocal boundary layer parameterization. *Reviews of Geophysics*, *32*, 363–403. https://doi.org/10.1029/94RG01872

Losch, M. (2008). Modeling ice shelf cavities in a *z* coordinate ocean general circulation model. *Journal of Geophysical Research*, *113*, C08043. https://doi.org/10.1029/2007JC004368

Losch, M., Menemenlis, D., Campin, J.-M., Heimbach, P., & Hill, C. (2010). On the formulation of sea-ice models. Part 1: Effects of different solver implementations and parameterizations. *Ocean Modelling*, *33*, 129–144.

Marshall, J., Adcroft, A., Hill, C., Perelman, L., & Heisey, C. (1997). A finite-volume, incompressible Navier-Stokes model for studies of the ocean on parallel computers. *Journal of Geophysical Research*, *102*, 5753–5766.

McDougall, T., Jackett, D., Wright, D., & Feistel, R. (2003). Accurate and computationally efficient algorithms for potential temperature and density of seawater. *Journal of Atmospheric and Oceanic Technology*, *20*(5), 730–741.

Millgate, T., Holland, P. R., Jenkins, A., & Johnson, H. L. (2013). The effect of basal channels on oceanic ice-shelf melting. *Journal of Geophysical Research: Oceans*, *118*, 6951–6964. https://doi.org/10.1002/2013JC009402

Nakayama, Y., Timmermann, R., Schröder, M., & Hellmer, H. (2014). On the difficulty of modeling Circumpolar Deep Water intrusions onto the Amundsen Sea continental shelf. *Ocean Modelling*, *84*, 26–34. https://doi.org/10.1016/j.ocemod.2014.09.007

Padman, L., Costa, D. P., Dinniman, M. S., Fricker, H. A., Goebel, M. E., Huckstadt, L. A., . . . van den Broeke, M. R. (2012). Oceanic controls on the mass balance of Wilkins Ice Shelf, Antarctica. *Journal of Geophysical Research*, *117*, C01010. https://doi.org/10.1029/2011JC007301

Paolo, F. S., Fricker, H. A., & Padman, L. (2015). Volume loss from Antarctic ice shelves is accelerating. *Science*, *348*(6232), 327–331. https://doi.org/10.1126/science.aaa0940

Pauling, A. G., Bitz, C. M., Smith, I. J., & Langhorne, P. J. (2016). The response of the Southern Ocean and Antarctic Sea ice to freshwater from ice shelves in an Earth system model. *Journal of Climate*, *29*(5), 1655–1672. https://doi.org/10.1175/JCLI-D-15-0501.1

Payne, A. J., Vieli, A., Shepherd, A. P., Wingham, D. J., & Rignot, E. (2004). Recent dramatic thinning of largest West Antarctic ice stream triggered by oceans. *Geophysical Research Letters*, *31*, L23401. https://doi.org/10.1029/2004GL021284

Pritchard, H. D., Ligtenberg, S. R. M., Fricker, H. A., Vaughan, D. G., van den Broeke, M. R., & Padman, L. (2012). Antarctic ice-sheet loss driven by basal melting of ice shelves. *Nature*, *484*(7395), 502–505.

Purkey, S. G., & Johnson, G. C. (2012). Global contraction of antarctic bottom water between the 1980s and 2000s. *Journal of Climate*, *25*(17), 5830–5844. https://doi.org/10.1175/JCLI-D-11-00612.1

Regan, H. (2017). *Modelling the sources, variability and fate of freshwater in the Bellingshausen Sea, Antarctica* (PhD thesis). Cardiff, UK: Cardiff University.

Rignot, E., Jacobs, S., Mouginot, J., & Scheuchl, B. (2013). Ice-shelf melting around Antarctica. *Science*, *341*(6143), 266–270.

Rignot, E., & Steffen, K. (2008). Channelized bottom melting and stability of floating ice shelves. *Geophysical Research Letters*, *35*, L02503. https://doi.org/10.1029/2007GL031765

Rye, C. D., Naveira Garabato, A. C., Holland, P. R., Meredith, M. P., George Nurser, A. J., Hughes, C. W., . . . Webb, D. J. (2014). Rapid sea-level rise along the Antarctic margins in response to increased glacial discharge. *Nature Geoscience*, *7*(10), 732–735.

Schodlok, M. P., Menemenlis, D., Rignot, E., & Studinger, M. (2012). Sensitivity of the ice-shelf/ocean system to the sub-ice-shelf cavity shape measured by NASA IceBridge in Pine Island Glacier, West Antarctica. *Annals of Glaciology*, *53*(60), 156–162.

Schoof, C. (2007). Ice sheet grounding line dynamics: Steady states, stability, and hysteresis. *Journal of Geophysical Research*, *112*, F03S28. https://doi.org/10.1029/2006JF000664

Shepherd, A., Wingham, D., & Rignot, E. (2004). Warm ocean is eroding West Antarctic Ice Sheet. *Geophysical Research Letters*, *31*, L23402. https://doi.org/10.1029/2004GL021106

Smith, J. A., Hillenbrand, C.-D., Kuhn, G., Klages, J. P., Graham, A. G., Larter, R. D., . . . Frederichs, T. (2014). New constraints on the timing of West Antarctic Ice Sheet retreat in the eastern Amundsen Sea since the Last Glacial Maximum. *Global and Planetary Change*, *122*, 224–237. https://doi.org/10.1016/j.gloplacha.2014.07.015

Stammer, D. (2008). Response of the global ocean to Greenland and Antarctic ice melting. *Journal of Geophysical Research*, *113*, C06022. https://doi.org/10.1029/2006JC004079

Steig, E. J., Ding, Q., Battisti, D., & Jenkins, A. (2012). Tropical forcing of Circumpolar Deep Water inflow and outlet glacier thinning in the Amundsen Sea Embayment, West Antarctica. *Annals of Glaciology*, *53*, 19–28.

St-Laurent, P., Klinck, J. M., & Dinniman, M. S. (2015). Impact of local winter cooling on the melt of Pine Island Glacier, Antarctica. *Journal of Geophysical Research: Oceans*, *120*, 6718–6732. https://doi.org/10.1002/2015JC010709

Thoma, M., Jenkins, A., Holland, D., & Jacobs, S. (2008). Modelling Circumpolar Deep Water intrusions on the Amundsen Sea continental shelf, Antarctica. *Geophysical Research Letters*, *35*, L18602. https://doi.org/10.1029/2008GL034939

Timmermann, R., Le Brocq, A., Deen, T., Domack, E., Dutrieux, P., Galton-Fenzi, B., . . . Smith, W. H. F. (2010). A consistent data set of Antarctic ice sheet topography, cavity geometry, and global bathymetry. *Earth System Science Data*, *2*(2), 261–273. https://doi.org/10.5194/essd-2-261-2010

Van Wessem, J., Reijmer, C., Morlighem, M., Mouginot, J., Rignot, E., Medley, B., . . . Van Meijgaard, E. (2014). Improved representation of East Antarctic surface mass balance in a regional atmospheric climate model. *Journal of Glaciology*, *60*(222), 761–770. https://doi.org/10.3189/2014JoG14J051

Wåhlin, A. K., Kalén, O., Arneborg, L., Björk, G., Carvajal, G. K., Ha, H. K., . . . Stranne, C. (2013). Variability of warm deep water inflow in a submarine trough on the Amundsen Sea Shelf. *Journal of Physical Oceanography*, *43*(10), 2054–2070. https://doi.org/10.1175/JPO-D-12-0157.1

Walker, D. P., Brandon, M. A., Jenkins, A., Allen, J. T., Dowdeswell, J. A., & Evans, J. (2007). Oceanic heat transport onto the Amundsen Sea shelf through a submarine glacial trough. *Geophysical Research Letters*, *34*, L02602. https://doi.org/10.1029/2006GL028154

Walker, D. P., Jenkins, A., Assmann, K. M., Shoosmith, D. R., & Brandon, M. A. (2013). Oceanographic observations at the shelf break of the Amundsen Sea, Antarctica. *Journal of Geophysical Research: Oceans*, *118*, 2906–2918. https://doi.org/10.1002/jgrc.20212

Webber, B. G. M., Heywood, K. J., Stevens, D. P., Dutrieux, P., Abrahamsen, E. P., Jenkins, A., . . . Kim, T. W. (2017). Mechanisms driving variability in the ocean forcing of Pine Island Glacier. *Nature Communications*, *8*, 14507.